

**Computational simulation of natural ventilation in a
laboratory model of a service building**

João Pedro Monteiro Pereira

Thesis to obtain the Master of Science Degree in

Mechanical Engineering

Supervisors: Prof. Pedro Jorge Martins Coelho

Prof. João Carlos Godinho Viegas

Examination Committee

Chairperson: Prof. Carlos Frederico Neves Bettencourt da Silva

Supervisors: Prof. Pedro Jorge Martins Coelho

Members of the Committee: Prof. José Manuel da Silva Chaves Ribeiro Pereira

November 2017

Acknowledgments

I would like to start by showing my gratitude to my supervisor, Prof. Pedro Coelho, for his guidance and support throughout this thesis and during the course, and also for the opportunity he gave me to work on this project and to have a scholarship.

I would like to express my utmost gratitude to my family, for their endless support during these years.

I'm also thankful to my closest friends. They were unconditionally present every time I needed and with them I shared some of the most important moments during my years at the University. A special thanks to Cristina for her advices and to Celmar for helping me in this last stage. Finally, to Amrin, my deep thanks, for the unforeseen friendship and for all the good times we've had throughout this thesis.

“In theory, there is no difference between theory and practice.

But in practice, there is.”

Jan L. A. van de Snepscheut

Abstract

The goal of the present thesis is to numerically investigate the flow and temperature fields in a laboratory model of a compartment in an office building. The motivation lies in a project concerned with the study of an innovative solution that optimizes the use of suspended ceiling (generally used for decorative purposes, mainly useless), passive and mechanical ventilation in the cooling process of an office, with the aim of reducing the overall energy consumption. Night cooling represents a way to accomplish that goal because we can take advantage of the relative cold outdoor temperature and cool the building thermal mass, reducing the air average temperature on the next working day. The problem is explored with a computational simulation using a CFD software, reproducing the scaled model. In a first stage the study examines the temperature distribution and the flow field of the model with a localized floor heat source. Subsequently, the flow field with forced ventilation without heat source. And finally, the influence of the gaps between the suspended ceiling and walls are analysed. The results indicate that the increased amount of exposed slab area contributes to lower the day peak indoor temperatures. Night cooling decreases the slab core temperature by 4.5 °C in about 6 hours. And the configuration for the gap of 90×125mm yields the best thermal comfort.

Key Words: Thermal Comfort, CFD, Buoyancy driven Ventilation, Enclosure, Suspended Ceiling, Night Cooling, Performance analysis

Resumo

O objetivo desta tese é investigar numericamente os campos de escoamento e temperatura num modelo laboratorial de um compartimento num edifício de escritórios. A motivação deve-se a um projeto destinado a estudar uma solução inovadora que otimiza o uso de tetos falsos (em geral utilizados para fins decorativos, tendo pouca utilidade), e de ventilação passiva e mecânica no processo de arrefecimento de um escritório, com o objetivo de reduzir o consumo energético global do edifício. O arrefecimento noturno representa uma forma de alcançar essa meta porque podemos tirar partido da temperatura relativamente fria do exterior e arrefecer a massa térmica do edifício, reduzindo a temperatura média do ar do dia de trabalho seguinte. O problema é explorado com uma simulação computacional usando software CFD que reproduz o modelo em escala. Numa primeira etapa, o estudo examina a distribuição de temperatura e o campo de escoamento do modelo na presença de uma fonte térmica localizada no pavimento, subsequentemente, o campo de escoamento introduzindo ventilação forçada sem fonte térmica, e finalmente, é analisada a influência de lacunas entre o teto falso e paredes. Os resultados indicam que um aumento na área exposta da laje contribui para reduzir as temperaturas máximas diurnas no interior do edifício. O arrefecimento noturno diminui a temperatura do núcleo da laje em 4,5 °C em cerca de 6 horas. A configuração para a lacuna de 90×125mm resulta no melhor conforto térmico.

Palavras-Chave: Conforto térmico, MFC, Ventilação induzida por Impulsão, Compartimento, Teto Falso, Arrefecimento Noturno, Análise de Desempenho

Table of Contents

Acknowledgments	ii
Abstract.....	iv
Resumo	v
Table of Contents.....	vi
List of Figures	viii
List of Tables.....	x
List of Acronyms	xi
Nomenclature	xii
1 Introduction	1
1.1 Aim and Objectives.....	4
1.2 Document structure	5
2 Literature review	6
2.1 Introduction.....	6
2.1.1 Buoyancy driven natural ventilation.....	6
2.1.2 Night cooling ventilation.....	10
3 Experimental Setup	13
4 Problem formulation.....	14
4.1 Introduction.....	14
4.2 Governing Equations	14
4.2.1 Reynolds Averaged Navier-Stokes Equations	16
4.2.1.1 Turbulence Modelling - RNG $k - \epsilon$ Model	16
4.2.1.2 Radiation Modelling	19
4.3 Nondimensional Numbers	21
4.4 External Boundary Conditions.....	23
5 Method	25
5.1 Introduction.....	25
5.2 Design Modeler	26
5.3 Mesh.....	28

5.3.1	Mesh Independence Study	29
5.4	General Solver Settings.....	32
5.4.1	Boundary conditions (BC).....	36
6	Simulation Results and Analysis.....	38
6.1	Introduction	38
6.2	Heating Period	38
6.3	Cooling Period	44
6.4	Suspended Ceiling Influence, HP.....	49
7	Conclusions and Future Work	53
7.1	Conclusions	53
7.2	Future work.....	54
8	References.....	55
9	Appendix.....	58
	Appendix 1	58
	Appendix 2	59

List of Figures

Figure 1.1 - Basic principle of night cooling.....	2
Figure 1.2 - ASHRAE Standard 55-2010, Acceptable operative temperature ranges for naturally conditioned spaces. Source: [11].....	4
Figure 2.1 - Buoyancy Natural Ventilation	7
Figure 2.2 - Natural ventilation in a single space driven by a point heat source	8
Figure 2.3 - Velocity distribution for different heat load layouts (a) front side and (b) back side of the room. The scale is in SI units. Source: [16].....	8
Figure 2.4 - Temperature contour at a vertical plane across the occupant. Source: [21].....	10
Figure 2.5- Percentage of energy savings by using night ventilation as a function of the duration of operation. Source: [27]	11
Figure 3.1 - Inside view of the reduced scale model.	13
Figure 4.1 - Heat transfer through a plane wall (1D)- Temperature profile and the equivalent thermal circuit.	23
Figure 5.1 – Geometry of CFD model	26
Figure 5.2 - Front view of the CFD geometry model with the corresponding dimensions in millimetres.	27
Figure 5.3 - Top view of the CFD geometry model with the corresponding dimensions in millimetres.	27
Figure 5.4 - Isometric view of the computational mesh	28
Figure 5.5 - Mesh view in the Plane $Y = 0.625\text{m}$, with detailed view on the heat source;	28
Figure 5.6 - Point 1 (0.375;0.625;0.2) middle of the model, Point 2 (0.375;0.2;0.2) corner of the model, Point 3 (0.375;0.625;0.375) middle of the plenum, respectively	29
Figure 5.7 - Simplified scheme of computational deviations for the same physical point (Red dot) depending on the size of the mesh; ANSYS FLUENT solver uses finite volumes cell centred	30
Figure 5.8 - Mesh Size influence - CFD Temperature vs Seconds, in three points. 12 hours of heating period. 1k = 1000.....	31
Figure 5.9 - Red Line: 2x0.5s + 99x1s + 2x100s + 5x300s + 69x600s; Blue Line: 3x100s + 5x300s + 69x600s; Green Line: 3x100s + 5x300s + 23x1800s; Period of heating (12h) with rising ambient temperature	34
Figure 5.10 - CFD Simulation Residuals, Stepping Method of the Figure 5.9 (blue line)	35

Figure 6.1 - Influence of the convection coefficient at the exterior face of the slab on the temperature at point 3, through the heating period (50W); The convection coefficient of the other wall remained equal to 3 W/m ² K.....	39
Figure 6.2 - Temperature in point 2, according to the thermal boundary condition (heat flux and convection coefficient) on the side walls and floor. Concerning the heat flux imposed only one simulation was performed; The dashed blue line is a virtual simulation with the same slope of the dashed purple, with the purpose of showing its initial behaviour.	39
Figure 6.3 - Difference between the measured and calculated temperature in the heating period at thermocouple 35 (plenum) for two days.	41
Figure 6.4 - Temperature difference, $\Delta T = T_{\text{measured}}/CFD - T_{\text{Lab}}$, for two days.	41
Figure 6.5 - Temperature contour profiles with radiation for twelve heating periods. Plane Y=0.625m. HP - Heating Period.....	42
Figure 6.6 - Vector distribution with radiation for two heating periods. Plane Y=0.625m.....	43
Figure 6.7 - Vector distribution with radiation for two heating periods. Plane X=0.375m.....	43
Figure 6.8 - Influence of radiation in the temperature distribution in the end of the heating period (12h); (a)-Simulation with Radiation; (b)-Simulation without radiation. Plane Y=0.625m.....	44
Figure 6.9 - Temperature contour profiles with radiation for twelve cooling periods. Plane X=0.375m. CP - Cooling Period.....	45
Figure 6.10 - Temperature contour profiles with radiation for twelve cooling periods. Plane Y=0.625m.	46
Figure 6.11 - Velocity vector for 60s of operation time (the average velocity in the occupation zone is 50cm/s). Plane Y=0.625m.	47
Figure 6.12 - Velocity vector for 60s of operation time, Plane Z=0.361m (plenum).	47
Figure 6.13 - CFD temperature in slab core (0.375; 0.625; 0.425) during one cycle (HP and CP)	48
Figure 6.14 – Location of the vertical measurement lines. Line 1 (0.375; 0.625; 0 : 0.45) Line 2 (0.375; 0.15; 0 : 0.45) Line 3 (0.65; 1.1; 0 : 0.45) Line 4 (0.2; 1.1; 0 : 0.45)	49
Figure 6.15 - Vertical temperature profiles along the four measurement lines for 5 minutes of operation time (HP), with the 5 different design scenarios.....	50
Figure 6.16 - Vertical temperature profiles along the four measurement lines for 12 hours of operation time (HP), with the 5 different design scenarios.....	50
Figure 6.17 - Temperature contours for the different 5 scenarios	52
Figure 9.1 – UDF function, ambient temperature vs hour of the day	58
Figure 9.2 – Difference in the CFD temperature at Thermocouple 67 according to different ambient temperatures	59

List of Tables

Table 3.1 - Dimensions of the gaps between the suspended ceiling and the surrounding walls for the different design scenarios.....	13
Table 4.1 - RNG model coefficients.....	19
Table 4.2 - Properties used for Adimensional Study, all the values are taken at mean temperature (reference T=300K) [30][31]; $\Delta T \approx \text{MaxTemp} (95) - \text{MinTemp} (25)$, velocity = 15cm/s (from simulation experience).....	22
Table 4.3 - Adimensional numbers inside the model.....	22
Table 5.1 - Description of the Figure 5.1	26
Table 5.2 - Mesh Size influence, Numerical difference of mass flow rate through the openings and the mean fluid temperature.....	31
Table 5.3 - General Fluent Solver Settings.....	32
Table 5.4 - Spatial and Temporal Formulation.....	33
Table 5.5 - Initial Solution Condition	33
Table 5.6 - Boundary Conditions set up	36
Table 5.7 - Properties of the materials used in the simulations; Specified thickness for the walls of concrete and XPS.....	37
Table 6.1 - Results of the fluid mean temperature and the mass flow rate at the slots in two heating periods for the different scenarios.	52

List of Acronyms

AC	Air-conditioning
ASHRAE	American Society of Heating, Refrigerating and Air-Conditioning Engineers;
BC	Boundary conditions
CFD	Computational Fluid Dynamics;
CFL	Courant-Friedrichs-Lewy Number
CP	Cooling Period
CPU	Central Process Unit
DNS	Direct Numeric Simulation;
HP	Heating Period
HVAC	Heating, ventilating and air conditioning
IAQ	Indoor Air Quality;
LES	Large Eddy Simulation;
LNEC	Laboratório Nacional de Engenharia Civil;
RANS	Reynolds Average Navier Stokes;
RAM	Random Access Memory
S2S	Surface to Surface Model
UDF	User Defined Function
XPS	Extruded Polystyrene Foam

Nomenclature

Roman Characters

a	- Absorption Coefficient	$[m^{-1}]$
Ar	- Archimedes Number	[-]
$C_{\varepsilon 1}$	- RNG $k - \varepsilon$ model constant	[-]
$C_{\varepsilon 2}$	- RNG $k - \varepsilon$ model constant	[-]
C_{μ}	- RNG $k - \varepsilon$ model constant	[-]
C_p	- Specific heat at constant pressure	$[J/(kg \cdot K)]$
COP	- Coefficient of Performance	[-]
D	- Material Derivative	[-]
E	- Emissive Power	$[W/m^2]$
g	- Gravity acceleration	$[m/s^2]$
g'	- Reduced Gravity	$[m/s^2]$
Gr	- Grashof Number	[-]
h	- Specific fluid enthalpy or Convection Coefficient	$[J/kg]$ or $[W/(m^2 \cdot K)]$
H	- Irradiation	$[W/m^2]$
J	- Radiosity	$[W/m^2]$
k	- Turbulent kinetic energy	$[m^2/s^2]$
m	- Mass	$[kg]$
\vec{n}	- Surface normal unit vector	[-]
Nu	- Nusselt Number	[-]

L	- Characteristic Length	[m]
p	- Pressure	[Pa]
P	- Modified Pressure	[Pa]
Pr	- Prandtl Number	[-]
P_k	- Production of turbulent kinetic energy	[W/m^2]
\vec{q}	- Heat flux vector	[W/m^2]
\vec{r}	- Position vector	[m]
R	- Additional term in the equation of dissipation rate	[m^2/s^4]
Ra	- Rayleigh Number	[-]
Re	- Reynolds Number	[-]
S	- Turbulence model parameter	[s^{-1}]
S_{ij}	- Average velocity field strain rate	[s^{-1}]
t	- Time	[s]
T	- Temperature	[K]
\vec{u}	- Velocity vector	[m/s]
\bar{u}	- Mean velocity	[m/s]
u'	- Instantaneous fluctuating velocity	[m/s]
\bar{u}	- Average velocity	[m/s]

Greek Characters

α	- Thermal diffusivity	[m^2/s]
β	- Thermal expansion	[K^{-1}]

γ	- Empirically constant in the equation dissipation rate	[-]
λ	- Thermal conductivity	[W/(m.K)]
λ_{ij}	- Bulk viscosity	[kg/(m.s)]
σ	- Stefan-Boltzmann constant	[W/(m ² .K ⁴)]
σ_s	- Scattering coefficient	[m ⁻¹]
δ_{ij}	- Kronecker delta function	[-]
ε	- Turbulent kinetic energy dissipation rate	[m ² /s ³]
ϵ	- Surface Emissivity	[-]
η	- Mean strain rate	[s ⁻¹]
η_0	- Constant in the equation dissipation rate	[-]
μ	- Fluid kinematic viscosity	[kg/(m.s)]
ν	- Fluid kinematic viscosity	[m ² /s]
ν_t	- Turbulent dynamic viscosity	[m ² /s]
ρ	- Fluid density	[kg/m ³]
σ_ε	- Turbulent kinetic energy dissipation rate Prandtl number	[-]
σ_k	- Turbulent kinetic energy Prandtl number	[-]
Φ	- Extensive property of the fluid or phase function	[-]
ϕ	- Intensive value of the fluid	[-]
τ_{ij}	- Viscous stress tensor	[-]
Δ	- Interval Difference	[-]
\forall	- Elementary volume	[m ³]

Exponents

$(\bar{\quad})$ - Reynolds time average

$(\quad)'$ - Reynolds fluctuation

$(\dot{\quad})$ - Flux

Subscripts

$(\quad)_0$ - Reference value

$(\quad)_i$ - i direction

$(\quad)_j$ - j direction

$(\quad)_k$ - k direction

$(\quad)_r$ - Variable surfaces r

$(\quad)_s$ - Variable in the surface s

$(\quad)_t$ - Turbulent Variable

$(\quad)_p$ - Relative to P node

1 Introduction

During the last decades, buildings represent the major consumers of energy, accounting for about 40% of the final energy consumed in Europe [1]. The main source of the problem is due to the constant rise, over the years, of the thermal loads in commercial buildings, mainly due to the arrival of office computers and lighting requirements; Heating, ventilating and air conditioning (HVAC) systems are therefore designed to neutralize these loads and to create a good comfortable indoor environment (supply fresh air to the occupants, remove heat, gases, and particulates from the building). [2][3].

It is crucial for buildings to have a good indoor air quality (IAQ). This is particularly true today since people, in industrialized countries, generally spend more than 90% of their time indoors [4]. Unhealthy buildings are sometimes related to high temperatures and poor ventilation.

Generally, there are three types of ventilation methods: mechanical (or forced) ventilation, natural ventilation and hybrid ventilation which is the combination of the first two methods [5]. Ventilation by mechanical means requires the use of a system that employs electric fans to drive a flow through a building. However, these mechanical systems consume large quantities of energy and have high maintenance costs and, for environmental reasons and the constant rising cost of energy, a suitable energy efficiency measure can contribute to a drastic decrease of the overall building energy consumption [6].

Notoriously, in Southern EU countries during daytime, HVAC systems operate under severe conditions as a result of the high environment temperatures, leading to a low energy efficiency ratio of the refrigeration cycle. The cycle efficiency or Coefficient of Performance (COP) is defined as follows:

$$COP = \frac{\text{Desired Output}}{\text{Required Input}} \quad (1.1)$$

Since COP is a ratio of cooling provided over the electrical energy consumed, higher COPs equate to lower operating costs. This means that operating at higher temperatures will imply lower COPs due to higher compressor work input required to maintain the same temperature. [7]

Thus, taking advantage of the relatively low ambient air temperature during the summer nights (when ambient temperature is lower than indoor temperature), there is a potential of using nocturnal ventilation (fan) in order to cool down the structural elements and thereby increase the energy efficiency of mechanical systems of a building. This strategy of night ventilation, in which the heat is transferred from the exposed elements to the circulating air, will have the opposite effect during daytime; the structural elements will be used as heat sink, Figure 1.1 - Basic principle of night cooling. [8]

This strategy is not so simple because each space has its own characteristics: location of the room (exposure by solar radiation) and its dimensions, vent positions and sizes; all these factors constitute the uniqueness of the building.

This work presents an innovative solution that uses the suspended ceiling and the plenum (space between the slab and the suspended ceiling) for cooling purposes. Different configurations of the length and width of the suspended ceiling will be studied to optimize the phenomenon of night cooling. Therefore, the best way to analyze these several design scenarios is to use a computer simulation, which can provide fast analysis with acceptable accuracy.

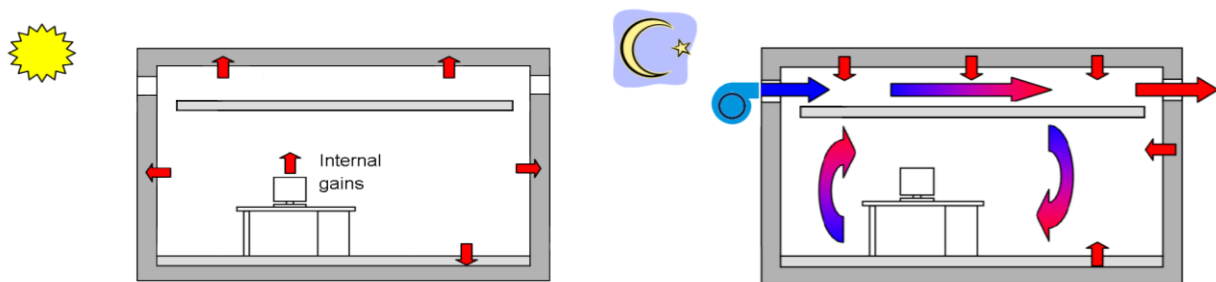


Figure 1.1 - Basic principle of night cooling

This numerical study is an additional work that aims to simulate an experimental project in which an office in reduced scale (1:7) is reproduced. The facility where the experimental set-up was constructed and installed belongs to LNEC – Laboratório Nacional de Engenharia Civil (Civil Engineering National Laboratory) in Lisbon. The numerical results will be compared with unpublished data from the experimental work, specially in the boundary conditions and point temperatures.

Obviously, to interpret the numerical results and in order to obtain the best results, we must realize the physical limitations/characteristics of the thermal comfort for the human body.

Thermal Comfort

The term thermal comfort is defined as “the state of mind that expresses satisfaction with the thermal environment”. This is the most accepted definition, but the concept presents several problems when translated into physical parameters. It not only involves physiologic but also psychological and subjective considerations; different people may feel thermally comfortable in totally different thermal environments [2]. That’s why, sometimes, it’s so difficult to find the ideal temperature for all the occupants in a certain space. For that reason, we must find a region acceptable to most of the occupants.

The way that our body controls the body temperature is complex and not yet fully understood. The body temperature is under, automatic control via hypothalamic regulation (center of the brain). Peripheral

receptors (skin) project to the hypothalamus the sensation of cold or warm. The system ensures that the body's core temperature is kept at approximately 37°C. The body's cooling function starts when the body's core temperature exceeds 37°C and its defense against the effect of cooling down starts when the skin temperature starts to fall below 34°C. This regulatory system is dependent on the following parameters. [9]

General Requirements when defining conditions for acceptable thermal comfort [2]:

1. Metabolic rate
2. Clothing insulation
3. Air speed
4. Radiant temperature
5. Air temperature
6. Humidity

Metabolic rate is the amount of heat released by the body depending on the amount of physical activity being performed. Most of the body's energy is released in the form of heat. The ASHRAE Standard 55-2010 express the metabolic rate in Met (1 Met = 58.15 W /m² of body surface). A typical normal adult has a body surface area of around 1.7 m², and with an activity level of 1 Met (seated relaxed) will thus have a heat loss of approximately 100W. Metabolic rate varies between individuals according to their age and sex.

This heat release, in an enclosed space, sets a circular air motion (induced by thermal buoyancy) that might cause draught. Draught is defined as an unwanted local cooling of the body caused by air movement. This body heat loss is dependent on the average air velocity, as well as the turbulence in the airflow and the temperature of the air. This is one of the most common causes of complaint in ventilated or air-conditioned buildings, derived from people's sensitivity in areas such as the face, hands and lower legs (unclothed parts of the body). [10]

Regarding the air temperature, it is acceptable to determine the allowable indoor operative temperatures from Figure 1.2; it is based on a global database of 21,000 measurements taken primarily in office buildings. This figure includes two sets of operative temperature limits, one for 80% acceptability and one for 90% acceptability. The 80% acceptability limits are for typical applications (metabolic rates ranging from 1.0 to 1.3 met). It is acceptable to use the 90% acceptability limits when a higher standard of thermal comfort is desired. [11]

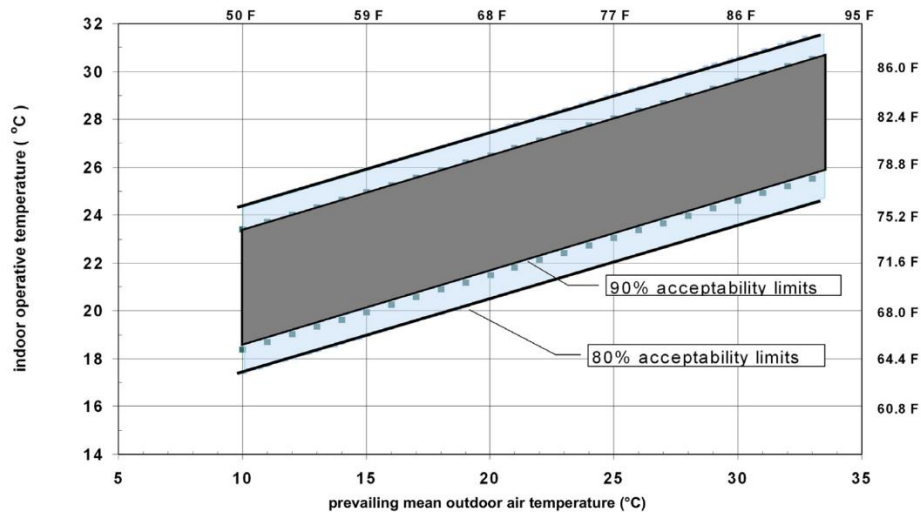


Figure 1.2 - ASHRAE Standard 55-2010, Acceptable operative temperature ranges for naturally conditioned spaces. Source: [11]

Regarding vertical air temperature difference, experiments performed by Olesen et al. [12] show that the temperature limit, between head and ankle level, for a person it is in a state of thermal neutrality should not exceed 3-4 K in spaces of high demands of thermal comfort. Only 5% of the population feels uncomfortable in this range. Therefore, 3°C air vertical temperature difference has been chosen as the ISO 7730 acceptance level for a sitting person at sedentary activity.

It is important to highlight that there are some studies, in the literature, that use bioclimatic charts as a preliminary analysis tool during the thermal comfort project. In this work, it will be not necessary to mention this topic due to the assumption that humidity is not involved.

1.1 Aim and Objectives

Summing up, the main objective conducted in this thesis is to study the flow field in a 3D compartment with a suspended ceiling of an office building using computational fluid dynamics (CFD) software. For this purpose, the CFD software from ANSYS Inc., called *Fluent*, is employed.

In particular, the present work investigates the influence of key CFD modeling issues, and provides guidance and reliability on the use of CFD for modeling flows in enclosures. These issues include the influence of initial solution, mesh influence, time step influence and the study of the flow field for natural and mechanical ventilation, through velocity vectors, temperature contours, air temperature gradients (stratification levels) and mass flow rates.

And finally, to investigate the performance of several designs of a suspended ceiling in a scaled office building. This objective considers the effect of changing the dimensions, length and width, of the suspended ceiling to investigate the performance of heat exchange between the plenum and occupied zone of the room. Whether the new design system is able to provide high air quality and a comforting environment in the occupied zone.

1.2 Document structure

The thesis is organized into seven chapters:

1-Introduction

This first chapter carries out an overview of the work developed throughout this thesis as well as the main objectives that were set. It also shows how the thesis is organized.

2-Literature review

This chapter contains a general literature review about the subject of buoyancy driven ventilation and night cooling in compartments, as well as previous studies done CFD.

3-Experimental Setup

The third chapter describes the most relevant characteristics of the experimental setup used by the analogous experimental project.

4-Problem formulation

Physics of the problem is discussed in this chapter. Describing the numerical modelling and the approximations used in the computational study.

5-Method

This chapter includes all the detailed characterization of the computational setup used in the numerical simulations.

6-Simulation Results and Analysis

In this chapter, CFD simulations are performed to generate the desired flow fields, for heating and cooling periods, and for different design scenarios of the suspended ceiling.

7-Conclusions and Future Work

Finally, in this chapter, we summarize and conclude the conducted work. Also, recommendations (to improve the energy efficiency of the building) for future work are presented.

2 Literature review

2.1 Introduction

There are barriers preventing the wide spread acceptance of natural ventilation. Firstly, there is a lack of knowledge regarding the airflow patterns, and secondly, a relatively low level of control compared with mechanical ventilation systems. It is desirable to be able to predict the performance of ventilation strategies at the design stage in order to know whether the strategy is practical or not. Different types of techniques, such as simple mathematical models, small-scale laboratory experiments, have been developed to study natural/mechanical displacement ventilation in buildings. Simple mathematical models can be used to predict the main parameters of natural ventilation flows (for example the ventilation rate through the building and the height of the fresh air zone for occupants), while the data produced by small-scale laboratory experiments are useful for visualizing the flow and validation of analytical models. However, CFD method provides detailed information, such as the detailed distributions of air temperatures and velocities, and is not costly, time-consuming and difficult to modify compared to the other methods.

So, this chapter will briefly review studies that were done in ventilation (natural/nocturnal), as well as some research on CFD in enclosures.

2.1.1 Buoyancy driven natural ventilation

The main driving force that causes natural ventilation through buildings is the pressure differential across the building envelope. This pressure difference can be generated mainly by two effects [13]:

- wind pressure, dynamic pressure variations can be due to the flow of the wind around a building and consequently can drive a flow through the building;
- thermal buoyancy, static pressure differences between the interior and exterior, e.g. windows, doors etc., of the building created naturally by density differences caused by a heat source inside the building. This pressure difference drives a flow (known as stack effect or chimney effect).

These effects can operate simultaneously in a building according to the strength of the prevailing wind and the temperature conditions.

The effect of wind pressure is a highly complex subject and generalizations in this field often lead to erroneous architectural strategies. Therefore, in this work, only the case of natural ventilation induced by a heat load, without wind, will be studied.

Buoyancy driven displacement ventilation occurs when fluid adjacent to a hot surface (e.g. occupants and electrical equipment) rises, forming a thermal plume. When a plume reaches the ceiling, it spreads out horizontally, forming a buoyant layer of warm air beneath the ceiling. This buoyant layer drives a displacement flow out through vents at ceiling level, Figure 2.1. This system takes advantage of the buoyancy forces to remove contaminants and heat from the occupied zone. The stronger the buoyancy flow, the stronger is the mixing level in the room. However, vertical stratification is developed creating a vertical temperature gradient in the room.

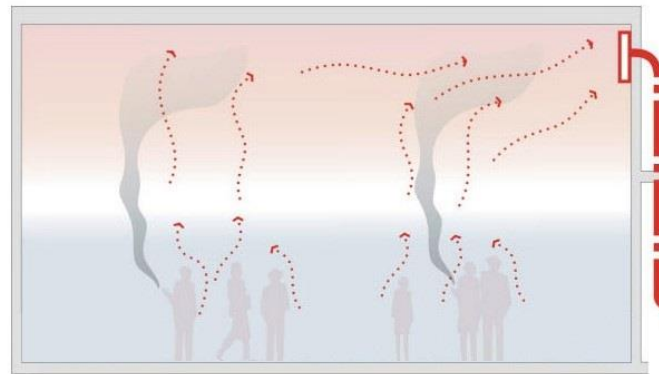


Figure 2.1 - Buoyancy Natural Ventilation

A theory for this type of ventilation was described by Linden [14], studying a heat source in a simple rectangular box, with one low opening in the floor and one in the ceiling (Figure 2.2). The heat source transfers heat from the surface to the adjacent air and a density difference is produced, creating a rising thermal plume which is surrounded by cooler ambient air. Assuming ρ_0 as the density of the ambient air, $\Delta\rho$ as the density difference between ambient air and air in the upper layer of the box, buoyancy can be interpreted as a reduced gravity, $g' = g\Delta\rho/\rho_0$, acting upwards. The density difference, forces dense fresh (ambient) air through the lower opening, and light fluid leaves through the upper, producing a stable interface at height $(H - h)$. Entrainment of the surrounding air occurs at the shear layer between the warm air in the plume and the ground (denoted by the horizontal arrows in Figure 2.2), which causes a reduction in the temperature difference with the increasing height of the plume and an increasing plume width.

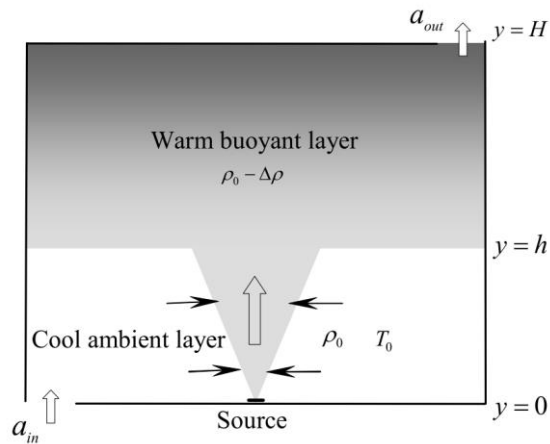


Figure 2.2 - Natural ventilation in a single space driven by a point heat source

On the experimental front, tests were made to better understand the underlying principles and characteristics of the regime:

Fitzgerald and Woods [15], focused their study on how the **airflow rate** varies according to the vent area/position and the heat load, in a room with a heat source at the floor and with two level vents. Concluding that the ventilation rate depends upon the strength of the heat source, the effective size of the vent openings and the vertical distance between the vents. In particular, appropriate control of the vent locations enables thermal comfort to be achieved.

According to [16], the **location of the heat sources** is very important for the air flow pattern and also for the thermal comfort. This study (experimental and numerical) with a diffuse suspended ceiling investigates four different heat load (80 W) distributions, including heat sources evenly distributed, located in the centre, located on the front side of the room and located on the back side of the room. A strong air recirculation occurs when the heat sources are placed on one side of the room and the direction of recirculation is opposite to the heat source location, as shown symbolically in Figure 2.3 (a) and (b). When the heat sources are located in the centre of the room, two air recirculation zones occur around the heat sources.

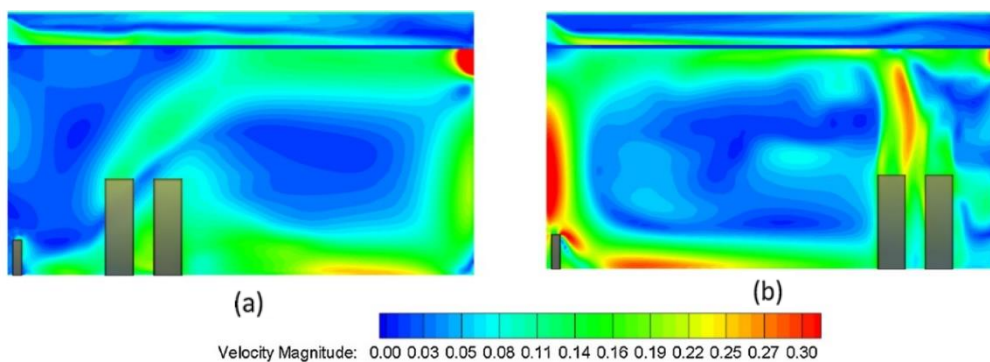


Figure 2.3 - Velocity distribution for different heat load layouts (a) front side and (b) back side of the room. The scale is in SI units. Source: [16]

On the numerical front, previous studies that used buoyancy driven flows in CFD state that this type of flows are notoriously difficult to model for the following reasons: small driving forces lead to numerical instabilities (of the order of 1.0 Pa) [17]; there is uncertainty regarding how to accurately model turbulence. Consequently, much validation work is needed to evaluate the ability of these codes to model such flows.

According to Cook et al. [18], they found out how important it is to select the appropriate turbulence model when simulating natural ventilation flows driven by buoyancy forces even in a very simple geometry. They compared, qualitatively and quantitatively, their CFD results with experimental data and the theoretical work of Linden [14]. The general flow patterns and direction of the flow agree well with the experimental work for RNG $k - \varepsilon$ and for the standard $k - \varepsilon$. The results further confirm, a general felt overview, that turbulence is difficult to model, especially buoyancy produced turbulence. Q. Chen [19], reinforced the study on the performance of different $k - \varepsilon$ models. One of the conclusions is that the standard $k - \varepsilon$ model is good, but RNG $k - \varepsilon$ model is slightly better for simulations of indoor airflow, claiming that the RNG model, handles stratification and swirl effects better than the standard $k - \varepsilon$ model. Furthermore, the standard $k - \varepsilon$ model is valid only in high Reynolds number flows, while the RNG model provides differential formulation for an effective viscosity in low Reynolds number flows.

A key consideration in our CFD modeling work is how to specify appropriate boundary conditions at the inlet and outlet locations of the enclosure. M. J. Cook, Y. Ji [20] studied the use of constant pressure boundary conditions imposed directly at the openings. A conclusion drawn is that is not required to explicitly model the air flow outside the building (physical areas to model effects of expansion and discharge), which would result in a computational overhead and could lead to errors if the conditions on the domain boundaries are not specified accurately. These constant boundary conditions at the openings still enable the effects of the buoyancy driving force established inside the space. Good agreement with experimental measurements indicate that this approach to modeling the boundary conditions is robust.

The performance of a diffuse ceiling ventilation system in a typical office room was studied by Jianhua Fan et al. [21]. In the experiments the air from the plenum leaks through holes in an aluminium profile. A thermal plume is created by two heat loads, pictured by an occupant and a window (Figure 2.4). This experiment with a heat source in an enclosure could leave an overview of how our flow, given by CFD results on an enclosure, could be.

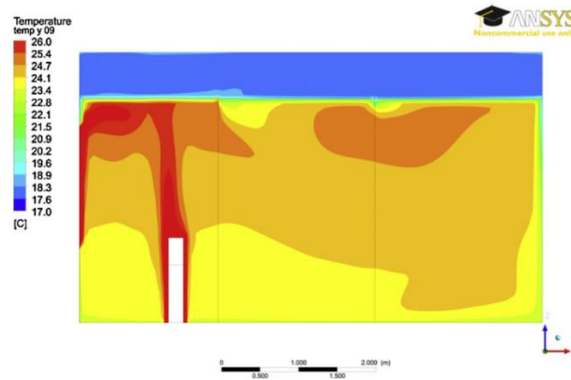


Figure 2.4 - Temperature contour at a vertical plane across the occupant. Source: [21]

It is interesting to note that the CFD approach has also been used for peculiar studies, such as a 100-year-old Buddhist temple, improving the building design and internal comfort by adopting night cooling ventilation and ceiling insulation [22].

2.1.2 Night cooling ventilation

As briefly mentioned in Chapter 1, during the summer season, night cooling ventilation draws the relatively cold outdoor air, fan-assisted, into the indoor space. The thermal air mass acts as a heat sink to cool down the indoor temperature of the building. This technique is more applicable to offices which are unoccupied during the night, so that relatively high air flows via mechanical means can be used to provide the maximum cooling effect, and the structure can be cooled efficiently.

During daytime, the pre-cooled thermal mass of the building is then able to temper the interior temperature during occupied hours, counteracting the build-up of heat due to interior loads. In this way, the internal temperature of the building is moderated; not getting as cold as the environment during the night-time, but also not reaching the high temperatures occurring during around noon and early afternoon hours.[23].

The effectiveness of night ventilation is strongly influenced by three main parameters [24]-[25]:

1)The relative difference between indoor and outdoor temperatures during the night period.

Having the fans drawing outside cool air to the interior forces an exchange between the air and building's thermal mass. The greater the temperature difference, the greater the heat flux and the efficiency of night ventilation.

2)The useful air flow rate applied during the night period.

Artmann et al. [25], performed a series of simulations with different night ventilation air change rates, clearly demonstrating that increased flow rates can significantly reduce the overheating degree hours (number of hours in the operating room with a temperature above 26 °C). However, there is a certain

value whereby the rate of airflow does not lead to further improvements. This critical air flow rate depends on the building construction and, of course, in the internal heat gains.

3)The thermal capacity of the building or heat gains.

The thermal mass of a building can be characterized by the ability of materials in the building to absorb heat during the day. High thermal mass means that the building materials induce high resistance to change in temperature. Consequently, an essential requirement, for night-time ventilative cooling, is a high thermal capacity of the building elements (e.g. ceiling, floor, walls) to store heat. The thermophysical properties must exhibit a proper density (ρ), high thermal capacity (C), and a high thermal conductivity value (λ), so that heat may be retained and dissipated during the specific time of heat charging and discharging, respectively. As a result, e.g. a wall with a low value of ($\rho C\lambda$) will have a low heat storage capacity, even though it may be quite thick [26].

According to the results of Geros et al. [24], the influence of thermal mass ($\rho C\lambda$) with night ventilation permits to delay the peak indoor temperature to about 3h after the peak outside temperature (14/15h), while the corresponding peak when no night ventilation is applied, is close to 1 h (16h). This time lag is actually desirable because the peak internal temperature occurs at the end of the workday when there are fewer occupants. Another conclusion drawn by the authors is that night cooling is efficient, and in their study, there is about 3°C (average) disparity compared to the case where no night ventilation techniques are applied.

Kolokotroni and Aronis [27], introduce some other variables, such as solar and internal gains, orientation, operation time for nocturnal ventilation and demonstrate that the lower the solar and internal gains, the more effective the night ventilation strategy is; a north orientation requires the minimum energy for cooling; and that the longer the operation, the better the benefits (Figure 2.5), although increasing more five hours of operation (7:00 pm to 7:00 am instead of 12:00 am to 7:00 am), according to their scenario, improves only 2% energy savings. Overall, optimizing the building design according to these parameters can cause an abatement of about 20-25% of the air conditioning energy consumption.

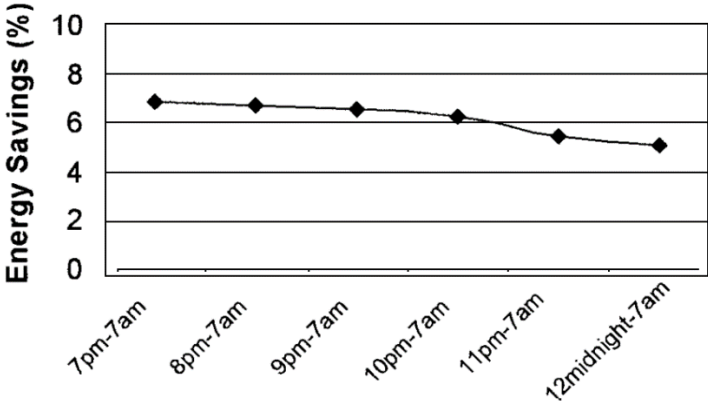


Figure 2.5- Percentage of energy savings by using night ventilation as a function of the duration of operation. Source: [27]

Several opinions converge in the sense that the greater the thermal mass of the building exposed to the airflow, the greater is the night cooling efficiency. However, there is a setback, in most modern constructions; there are components (e.g. suspended ceiling), that act as insulators, preventing the thermal mass to be exposed to the living space, which influences the desired heat exchange (not allowing the heat exchange in an efficient manner). Høseggen et al. [28] also pointed out that the suspended ceiling decreases the potential of night ventilation significantly and also increases the number of hours with excessive temperature considerably. However, some studies have demonstrated that a suspended ceiling without full coverage improves thermal cooling. Weitzmann [29] show that even a large covering (83%) of the ceiling surface area, still gives significant cooling capacity (70%) compared with the uncovered ceiling, for the same temperature difference between mean fluid temperature and room operative temperature.

It is also interesting to mention that even though the literature is poor in numerical studies on our topic, the conclusions of the few existing works show that in order to improve the predictions of CFD modelling with internal heat sources, it is recommended to take special attention to the following issues: turbulence modelling (RNG $k - \varepsilon$), temporal/spatial discretization, radiation modelling, and to thermal and momentum boundary conditions.

3 Experimental Setup

This chapter summarily describes the analogous experimental arrangement, which the computational work aims to simulate. It consists of a scale model (Figure 3.1) of an office with dimensions of $0.75m \times 1.25m \times 0.4m$, orthogonal shape. The model is assumed to be “occupied” from 8:00 to 20:00, and a heat source is used to simulate the heat release due to the occupants and equipment. Physically consists in a cylindrical electric resistance with a length of 1.20m shape, placed near a corner relative to the floor, and emitting in this period 30/50/100 Watts. This heating period is followed by 12 h (20:00 to 8:00) of night cooling, without thermal load, using a fan in one of the openings (the closest to the load) operating with a velocity magnitude of 6/8/10m/s. The openings are placed in between the ceiling and the suspended ceiling, at opposite sides walls. The temperature of the ambient air of the model is the laboratory temperature and will be varying according to the hour of the day, having its peak close to end of the heating period.

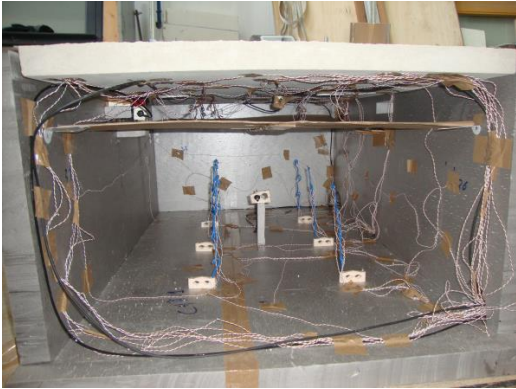


Figure 3.1 - Inside view of the reduced scale model.

The reduced scale model allows to change the size of the peripheral gap between the suspended ceiling (made of cardboard) and the surrounding walls, and the tests done to date have the following gaps:

Table 3.1 - Dimensions of the gaps between the suspended ceiling and the surrounding walls for the different design scenarios.

	Scenario 1	Scenario 2	Scenario 3	Scenario 4	Scenario 5	Scenario 6
Length (mm)	32	64	90	240	0	without Suspended Ceiling
Width (mm)	32	64	125	120	0	

In this thesis, the numerical study will be modeled according to the experimental arrangement using 50 Watts of power and an insufflation velocity of 8m/s. The scenario 2 (64mm*64mm) was chosen as a starting point, and the ambient temperature simulated as a sinusoidal ranging from 23 °C to 25.4 °C. All the scenarios will be studied (for natural ventilation) in the heating period except for the Scenario 5 (no gap).

4 Problem formulation

4.1 Introduction

Before proceeding with the method and results of numerical simulations, it is worthwhile to describe the mathematical modelling involved and the conservation equations that govern the flow in the enclosure. This chapter begins with a description of these equations. Subsequently, the description of the models used in the computational work, in particular, the RNG k-ε turbulence model, and the Surface to Surface (S2S) model for radiation modelling. Following this, dimensionless quantities give insight into the behavior of the fluid. Finally, the theoretical boundary conditions for the external walls of the enclosure, are presented.

4.2 Governing Equations

In order to obtain the basic transport equations, in their differential form, one can start from the Reynolds Transport Theorem, whose formulation, in the integral form, is as follows:

$$\frac{D}{Dt} \Phi = \frac{\partial}{\partial t} \iiint \rho \phi dV + \iint \rho \phi (\vec{u} \cdot \vec{n}) dS \quad (4.1)$$

Where ρ is the density, \vec{u} is vector of the velocity in the surface S , \vec{n} is the outward normal unit vector in the elementary surface dS ; Φ can be any property of the fluid (mass, momentum, energy, etc.) and $\phi = d\Phi/dm$ is the intensive value, or the amount of Φ per unit mass in any small element of the fluid ($dm = \rho dV$).

The dynamic behaviour of the fluid is ruled by the following three conservation equations:

The **conservation of mass**, in one control volume, is expressed by the continuity equation:

$$\frac{\partial \rho}{\partial t} + \frac{\partial(\rho u_j)}{\partial x_j} = 0 \quad (4.2)$$

where u_j stands for the component of velocity in the x_j coordinate directions, ρ and t denote density and time, respectively. This equation is valid for compressible and incompressible flows.

The **conservation of momentum** equations in cartesian coordinates can be derived from Newton's second law:

$$\underbrace{\frac{\partial}{\partial t}(\rho u_i)}_{\text{Unsteady term}} + \underbrace{\frac{\partial}{\partial x_j}(\rho u_j u_i)}_{\text{Convection}} = \underbrace{\rho g_i}_{\text{Buoyancy}} - \underbrace{\frac{\partial p}{\partial x_i}}_{\text{Pressure gradient}} - \underbrace{\frac{\partial \tau_{ij}}{\partial x_j}}_{\text{Diffusion}} \quad (4.3)$$

This is usually called the Navier-Stokes equation of motion; g_i is the gravitational acceleration, p is the static pressure, and τ_{ij} is the viscous stress tensor, which can be expressed in terms of velocity gradients using Stokes' law:

$$\tau_{ij} = -\mu \left(\frac{\partial u_i}{\partial x_j} + \frac{\partial u_j}{\partial x_i} \right) - \mu \lambda_{ij} \delta_{ij} \frac{\partial u_k}{\partial x_k} \quad (4.4)$$

μ is the dynamic viscosity of the fluid; λ_{ij} is volume viscosity (also called second viscosity or bulk viscosity) important where fluid compressibility is essential, common approximation $\lambda_{ij} = -\frac{2}{3}$; and δ_{ij} is Kronecker's delta function¹.

The **conservation of energy**² (in terms of specific enthalpy), which can be described by the first law of thermodynamics, is expressed as:

$$\underbrace{\frac{\partial}{\partial t}(\rho h)}_{\text{Unsteady term}} + \underbrace{\frac{\partial}{\partial x_j}(\rho u_j h)}_{\text{Convection}} = \underbrace{-\frac{\partial q_j}{\partial x_j}}_{\text{Diffusion}} + \underbrace{\tau_{ij} \frac{\partial u_i}{\partial x_j}}_{\text{Dissipation}} + \underbrace{\left(\frac{\partial p}{\partial t} + u_j \frac{\partial p}{\partial x_j} \right)}_{\text{Compressibility effect}} \quad (4.5)$$

Where h stands for the enthalpy of the fluid:

$$\rho dh = (1 - \beta T) dp + \rho C_p dT \quad (4.6)$$

And q_j is the heat flux due to conduction, which is expressed in terms of the temperature gradient using Fourier's law:

$$q_j = -\lambda \frac{\partial T}{\partial x_j} \quad (4.7)$$

λ is the heat conductivity of the fluid, and T the temperature of the fluid.

These governing equations are often used to solve laminar flows, but they are also used to solve complicated turbulent flows, numerically, using techniques, such as CFD. The most accurate means of modeling fluid flow numerically is the Direct Numerical Simulation (DNS). There are two main advantages of using DNS, accurate governing equations without any turbulence model and detailed results, which are helpful for understanding the behaviour of turbulence. However, the mesh size of the

¹ $\delta_{ij} = 1$ if $i = j$ and $\delta_{ij} = 0$ if $i \neq j$

² Radiation neglected

domain needs to be small enough to model all the range of turbulent eddies within the domain (Murakami 1997). This is not feasible for indoor environment spaces because it requires very high computing time, a large memory (RAM), which is prohibitive for the current computers, and it is also expensive for simulations of this kind.

One of the approaches to reduce computational effort is using large eddy simulations (LES), in which the small eddies are filtered and are modeled independently by some simple models. The LES method uses less resolution than DNS solving but still requires extremely fine grids and too much computational time. The "Reynolds averaged Navier-Stokes equations", which were derived by Reynolds through averaging the Navier-Stokes equations, are most often used for solving turbulent flows.

4.2.1 Reynolds Averaged Navier-Stokes Equations

This is a method to reduce the computing cost, the fluid properties are modeled by time-averaged mean quantities and the effects of their fluctuations.

Performing these substitutions and applying time-averaging into the equations (4.2)-(4.6), transforms them into the well-known Reynolds Averaged Navier-Stokes (RANS) Equations, where the density fluctuations are neglected.

$$\frac{\partial \bar{p}}{\partial t} + \frac{\partial}{\partial x_j} (\bar{\rho} \bar{u}_j) = 0 \quad (4.8)$$

$$\begin{aligned} \frac{\partial}{\partial t} (\bar{\rho} \bar{u}_i) + \frac{\partial}{\partial x_j} (\bar{\rho} \bar{u}_j \bar{u}_i) = \bar{\rho} g_i - \frac{\partial \bar{p}}{\partial x_i} - \frac{\partial}{\partial x_i} \left(\frac{2}{3} \mu \frac{\partial \bar{u}_k}{\partial x_k} \delta_{ij} \right) \\ + \frac{\partial}{\partial x_j} \left[\mu \left(\frac{\partial \bar{u}_i}{\partial x_j} + \frac{\partial \bar{u}_j}{\partial x_i} \right) \right] - \frac{\partial}{\partial x_j} (\bar{\rho} \bar{u}_j' u_i') \end{aligned} \quad (4.9)$$

$$\frac{\partial}{\partial t} (\bar{\rho} \bar{T}) + \frac{\partial}{\partial x_j} (\bar{\rho} \bar{u}_j \bar{T}) = \frac{\partial}{\partial x_j} \left(\frac{\mu}{Pr} \frac{\partial \bar{T}}{\partial x_j} \right) - \frac{\partial}{\partial x_j} (\bar{\rho} \bar{u}_j' T') \quad (4.10)$$

Pr is the Prandtl number, $Pr = \mu C_p / \lambda$. number (a relative measure of molecular momentum diffusivity and molecular thermal diffusivity).

4.2.1.1 Turbulence Modelling - RNG $k - \varepsilon$ Model

As a result of the time averaging, two unknown terms have been introduced: the turbulent momentum flux, or the Reynolds stress, $\bar{\rho} \bar{u}_j' u_i'$, and the turbulent heat flux, $\bar{\rho} \bar{u}_j' T'$. These terms must be related to known quantities via a turbulence model before a closed solution of the above equation system becomes

possible. A common approximation used by turbulence models is the Boussinesq hypothesis³, which relates the Reynolds stresses to the rate of mean strain, through the turbulent viscosity ν_t :

$$-\overline{u_j' u_i'} = \nu_t \left(\frac{\partial \bar{u}_i}{\partial x_j} + \frac{\partial \bar{u}_j}{\partial x_i} \right) - \frac{2}{3} \delta_{ij} \left(k + \nu_t \frac{\partial \bar{u}_k}{\partial x_k} \right) \quad (4.11)$$

$$-\overline{u_j' T'} = \frac{\nu_t}{Pr_t} \frac{\partial \bar{T}}{\partial x_j} \quad (4.12)$$

$$\nu_t = C_\mu \frac{k^2}{\varepsilon} \quad (4.13)$$

where Pr_t is the turbulent Prandtl number, k and ε are the kinetic energy of the turbulent fluctuations and the turbulent dissipation rate, respectively, which are defined as:

$$k = \overline{u_i' u_i'} / 2 \quad (4.14)$$

$$\varepsilon = \nu \frac{\partial u_i'}{\partial x_j} \frac{\partial u_i'}{\partial x_j} \quad (4.15)$$

The k and ε equations can be derived using certain model assumptions.

In numerical simulation of natural convection, where temperatures and velocities variations are small, the density differences are small, so the flow is treated as incompressible and can be modeled using the **Boussinesq approximation**⁴. This is a usually approach to get faster convergence in natural convection flow.

The fluid properties ρ , μ , and Prandtl are treated as constants in all solved equations except for the buoyancy term in the momentum equation. The thermal expansion coefficient, β , is:

$$\beta = -\frac{1}{\rho} \left(\frac{\partial \rho}{\partial T} \right)_p \approx \frac{1}{\rho_0} \frac{\rho_0 - \rho}{T_0 - T} \quad (4.16)$$

³ The Boussinesq hypothesis states that the Reynolds stresses are proportional to the local mean flow strain rate $\left(\frac{\partial \bar{u}_i}{\partial x_j} + \frac{\partial \bar{u}_j}{\partial x_i} \right)$

⁴ The Boussinesq approximation, modelling buoyancy-driven flows, is generally valid as long as the temperature variation of the fluid domain is $\Delta T < 30^\circ\text{C}$ [6]. In building simulations, the temperature differences in air are usually small and the density variation can be ignored. Therefore, the Boussinesq approximation is assumed to be accepted.

So, the density can be represented as:

$$\rho \approx \rho_0[1 - \beta(T_0 - T)] \quad (4.17)$$

Where: ρ_0 [kg/m^3], β [$1/K$] are the density and the coefficient of thermal expansion at a reference temperature T_0 [K]; which is usually taken as the average temperature in an enclosure. T is the local temperature of the fluid [K]

Under this approximation the governing equations with the RNG $k - \varepsilon$ model (3 conservation equations + 2 $k - \varepsilon$ equations) can be written as:

$$\frac{\partial(u_j)}{\partial x_j} = 0 \quad (4.18)$$

$$\frac{\partial u_i}{\partial t} + \frac{\partial}{\partial x_j}(u_j u_i) = -g_i \beta (T - T_0) - \frac{1}{\rho_0} \frac{\partial P}{\partial x_i} - \frac{\partial}{\partial x_j} \left[(v + v_t) \left(\frac{\partial u_i}{\partial x_j} + \frac{\partial u_j}{\partial x_i} \right) \right] \quad (4.19)$$

$$\frac{\partial T}{\partial t} + \frac{\partial}{\partial x_j}(u_j T) = \frac{\partial}{\partial x_j} \left[\left(\frac{v}{Pr} + \frac{v_t}{Pr_t} \right) \frac{\partial T}{\partial x_j} \right] \quad (4.20)$$

Where the overbar, to denote mean values, was omitted for simplicity.

P is considered a modified pressure: $P = p - \rho_0 g_i x_i$

The equation for the turbulent kinetic energy k written is as follows:

$$\underbrace{\frac{\partial k}{\partial t}}_{\text{Rate of increase}} + \underbrace{\frac{\partial}{\partial x_j}(u_j k)}_{\text{Convective transport}} = \underbrace{\frac{\partial}{\partial x_j} \left[\left(v + \frac{v_t}{\sigma_k} \right) \frac{\partial k}{\partial x_j} \right]}_{\text{Diffusive transport}} + \underbrace{P_k}_{\text{Rate of production}} - \underbrace{\varepsilon}_{\text{Rate of destruction}} \quad (4.21)$$

Where, the production of turbulent kinetic energy, is:

$$P_k = v_t \left(\frac{\partial u_i}{\partial x_j} + \frac{\partial u_j}{\partial x_i} \right) \frac{\partial u_j}{\partial x_i} - \frac{2}{3} k \frac{\partial u_i}{\partial x_i} = v_t S_{ij} S_{ij} - \frac{2}{3} k \frac{\partial u_i}{\partial x_i} \quad (4.22)$$

The last term is zero for incompressible flow, since the divergence of the velocity $\left(\frac{\partial u_i}{\partial x_i} \right)$ is zero.

And finally, the transport equation for the dissipation rate is:

$$\underbrace{\frac{\partial \varepsilon}{\partial t}}_{\text{Rate of increase}} + \underbrace{\frac{\partial}{\partial x_j}(u_j \varepsilon)}_{\text{Convective transport}} = \underbrace{\frac{\partial}{\partial x_j} \left[\left(\nu + \frac{\nu_t}{\sigma_\varepsilon} \right) \frac{\partial \varepsilon}{\partial x_j} \right]}_{\text{Diffusive transport}} + \underbrace{C_{\varepsilon 1} \frac{\varepsilon}{k} P_k}_{\text{Rate of production}} - \underbrace{C_{\varepsilon 2} \frac{\varepsilon^2}{k}}_{\text{Rate of destruction}} + \underbrace{R}_{\text{Additional term related to mean strain \& turbulence quantities}} \quad (4.23)$$

Where R is defined as:

$$R = - \frac{\eta(1 - \eta/\eta_0) P_k \varepsilon}{(1 + \gamma \eta^3) k} \quad (4.24)$$

$$\eta = S \frac{\varepsilon}{k} ; S = \sqrt{2 S_{ij} S_{ij}} ; S_{ij} = \sqrt{\frac{1}{2} \left(\frac{\partial u_i}{\partial x_j} + \frac{\partial u_j}{\partial x_i} \right)^2} \quad (4.25)$$

The parameter η is the ratio of the turbulent to mean strain time scale. The remaining constants are given in Table 4.1.

Table 4.1 - RNG model coefficients.

Constant	Value
C_μ	0.0845
$C_{\varepsilon 1}$	1.42
$C_{\varepsilon 2}$	1.68
σ_k	0.719
σ_ε	0.719
η_0	4.38
γ (empiracally)	0.012

4.2.1.2 Radiation Modelling

By using the Surface to Surface (S2S) model, we limit ourselves by ignoring any absorption, emission, or scattering of radiation, therefore, only "surface-to-surface" radiation need be considered for analysis. The main advantage of using this model is the simplicity and convenience of not having a participant media, thus, it is appropriate for our problem.

The radiation exchange in an enclosure regulated by the S2S model assumes that all surfaces are diffuse and grey. For a diffuse surface, the reflectivity is independent of the outgoing (or incoming) directions. And in a grey surface, emissivity and absorptivity are independent of the wavelength.

The radiative energy flux leaving a given surface s (Radiosity, J_s):

$$J_s = E_s + \rho_s H_s \quad (4.26)$$

is composed of directly emitted ($E_s = \epsilon_s \sigma T_s^4$) and reflected (fraction of the irradiation⁵, H_s) energy.

The energy exchange between two surfaces depends in part on their size, separation distance, and orientation. These parameters are accounted by a geometric function called a "view factor". Therefore, the incident energy flux (H_s) can be expressed in terms of the energy flux leaving all other surfaces (r) as:

$$A_s H_s = \sum_{r=1}^N A_r J_r F_{rs} \quad (4.27)$$

The view factor between two finite surfaces is the fraction of energy leaving surface r that is incident on surface s and is given by:

$$F_{rs} = \frac{1}{A_r} \int_{A_r} \int_{A_s} \frac{\cos \theta_r \cos \theta_s}{\pi r^2} \delta_{rs} dA_r dA_s \quad (4.28)$$

where δ_{rs} is determined by the visibility of dA_s to dA_r . $\delta_{rs} = 1$ if dA_s is visible to dA_r and 0 otherwise. For our enclosure with N surfaces, using the view factor reciprocity relationship gives:

$$A_r F_{rs} = A_s F_{sr} \quad \text{for } r = 1, 2, 3, \dots, N \quad (4.29)$$

Thus:

$$H_s = \sum_{r=1}^N F_{sr} J_r \quad (4.30)$$

And finally, the radiosity can be expressed as:

$$J_s = E_s + \rho_s \sum_{r=1}^N F_{sr} J_r \quad (4.31)$$

This represents N equations, which can be adjusted into a matrix form as

$$\mathbf{KJ} = \mathbf{E} \quad (4.32)$$

where \mathbf{K} is an $N \times N$ matrix.

⁵ Energy flux incident on the surface from the surroundings

As compared to other radiation models, the S2S model is solved by a fast-direct method, although the view factor calculation itself is CPU-intensive. The storage and memory requirements increase very rapidly as the number of surface faces increases.

4.3 Nondimensional Numbers

In general, it is convenient to use dimensionless numbers in order to describe the physical phenomena. The relevant nondimensional quantities related to buoyancy are the Grashof, Reynolds, Prandtl, and Rayleigh numbers. The values and combinations of these numbers will characterize the problem. Equations (4.33) through to (4.36) show the definition of these quantities.

$$Gr = \frac{g \beta L^3 \rho^2 \Delta T}{\mu^2} \quad (4.33)$$

$$Re = \frac{u_\infty L}{\nu} \quad (4.34)$$

$$Ar = Gr / Re^2 = \frac{g \beta L \Delta T}{u_\infty^2} \quad (4.35)$$

$$Ra = Pr * Gr = \frac{g \beta \Delta T L^3}{\mu \alpha} \quad (4.36)$$

Where α is the thermal diffusivity, which is defined as: $\alpha = \frac{\lambda}{\rho c_p}$

In problems involving natural or free convection, redistribution of energy is mainly due to the force of gravity acting on a fluid of non-uniform density and causing fluid motion. In mixed (i.e. free and forced) convection, the importance of buoyancy forces can be measured by the ratio of Grashof to Reynolds numbers.

Archimedes number (4.35) represents the ratio between buoyancy and inertial forces, so if it largely exceeds unity, it is reasonable to assume that the flow is dominated by buoyancy. Alternatively, if the ratio is very small, buoyancy forces may be ignored.

In natural convection problems, the strength of buoyancy-induced flow can be measured by the Rayleigh number stated in (4.36). Rayleigh numbers less than 10^8 usually indicate laminar flow, with the onset of turbulence occurring over the range $10^8 < Ra < 10^{10}$.

It is difficult to define the two reference parameters (characteristic length, L , and temperature difference, ΔT) in order to assess the value of the Rayleigh number in our case. In general, the height of the cavity is considered as characteristic length, while the reference difference temperature is based on the maximum difference temperature within the solution domain.

The assumed air properties for this calculation are summarized in Table 4.2.

Table 4.2 - Properties used for Adimensional Study, all the values are taken at mean temperature (reference $T=300K$) [30][31]; $\Delta T \approx \text{MaxTemp} (95) - \text{MinTemp} (25)$, velocity = 15cm/s (from simulation experience)

Typical values	($T_{ref} = 300K$)	Units
ρ	1.22	$Kg/(m^3)$
λ	0.02624	$W/(m K)$
μ	1.846×10^{-5}	$N.s/(m^2)$
Pr	0.712	-
α	22.07×10^{-6}	m^2/s
C_p	1.0049	$KJ/(Kg.K)$
β	3.33×10^{-3}	$1/K$
L	0.4	m
ΔT	70	K
u	0.15	m/s

It is important to highlight that ΔT is different from the Boussinesq approximation ($\Delta T^6 < 30^\circ C$) previously described because we are referring to the temperature variation in a small layer surrounding the heat source ($T \approx 95$, i.e. due to the emission of 50W in a small load) and the average temperature in the domain.

Table 4.3 - Adimensional numbers inside the model

Gr	6.4×10^8
Gr/Re^2	40.6
Ra	4.5×10^8

The results of Table 4.3 tell that the flow, inside the model, is definitely dominated by buoyancy forces ($Gr/Re^2 \gg 1$) which indicates that buoyancy should be included in the CFD model; and is most likely a turbulent, strong buoyant flow.

⁶ This difference is due to temperature variations that occur mainly in the domain.

4.4 External Boundary Conditions

To prescribe the wall boundary conditions, in the next section, we need to define and predict what will be the theoretical values for the external convection coefficient⁷.

The general case for our problem is a plane wall separating two fluids of different temperatures. Heat transfer is mainly transferred in one direction occurring convection from the hot fluid at $T_{\infty,1}$ to one surface of the wall at $T_{s,1}$, by conduction through the wall, and by convection from the other surface of the wall at $T_{s,2}$ to the cold fluid at $T_{\infty,2}$. This process is represented in Figure 4.1. [32]

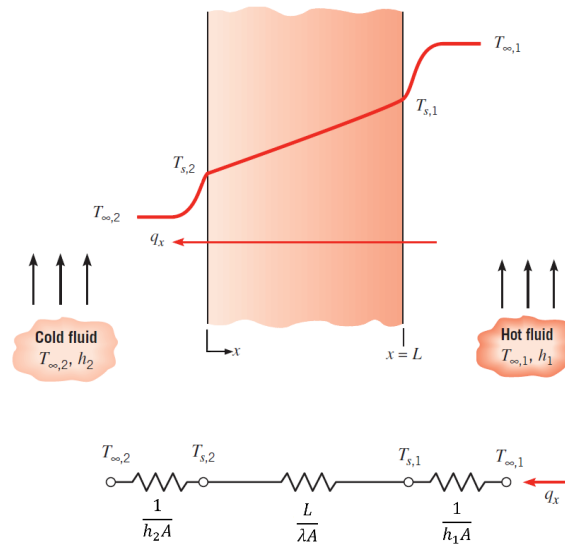


Figure 4.1 - Heat transfer through a plane wall (1D)- Temperature profile and the equivalent thermal circuit.

The heat transfer rate can be derived from the equivalent thermal circuit of the Figure 4.1 and expressed as:

$$q_x = \frac{T_{\infty,1} - T_{\infty,2}}{R_{tot}} \quad (4.37)$$

$$R_{tot} = \frac{1}{h_1 A} + \frac{L}{\lambda A} + \frac{1}{h_2 A} \quad (4.38)$$

Where λ is the thermal conductivity of the wall material, A is the area of the wall normal to the direction of heat transfer, h_1 and h_2 represents the convection coefficients, in the interior and exterior of the wall, respectively. h_1 is computed by the CFD solver and h_2 must be predicted to be imposed as a boundary condition. For our case, the coefficients for the exterior walls (Side Walls, Floor and Ceiling) are determined according to [32] and defined as:

⁷ This analysis neglects radiation

Side Walls – Vertical Plate

Mean properties of the outside flow:

$$\Delta T = T_s - T_\infty; T_{s,2}^8 \approx 26 \text{ }^\circ\text{C}; T_{\infty,2} = 23 \text{ }^\circ\text{C}; Pr, \nu, \alpha, \lambda, \beta (T_{film} = 300\text{K})$$

The correlation for the mean Nusselt Number in a vertical plate is recommended by Churchill and Chu:

$$\overline{Nu}_L = \frac{\bar{h} L}{\lambda} = \left\{ 0.825 + \frac{0.387 Ra_L^{1/6}}{\left[1 + (0.492/Pr)^{9/16} \right]^{8/27}} \right\}^2 \quad (4.39)$$

Where: $L = 0.40 \text{ m}$ (Height of the plate); $Ra_L = 2.05 * 10^7$

Resulting the mean convection number: $\bar{h} \approx 3 \text{ W/m}^2\text{K}$

Floor and Outside Face Slab - Upper Surface of heated Plate or Lower Surface of Cooled Plate;

$$\overline{Nu}_L = 0.15 Ra_L^{1/3} \quad (10^7 \lesssim Ra_L \lesssim 10^9, \text{ all } Pr) \quad (4.40)$$

Where: $L = 1.25 \text{ m}$ (Length of the plate); $Ra_L = 2.67 * 10^8$

Resulting: $\bar{h} \approx 3 \text{ W/m}^2\text{K}$

⁸ Typical temperature value from experimental results for the exterior walls

5 Method

5.1 Introduction

The improvement in computer power since the 1970s has led to the fast development of CFD. In particular, over the last 20 years, CFD made it possible to solve problems for a wide range of engineering applications. The main advantage was the possibility of analyzing the results (flow velocity, pressure, temperature, heat transfer etc.) in a relatively short period of time with a much less labor intensity and, therefore, leads to a reduction in costs. As a result, CFD is now an established industrial design tool, which can be used in helping to reduce design timescales and improving processes throughout the engineering world.

CFD is a numerical method of solving the governing equations (RANS equations and turbulence models as well as the radiative transfer model) determining a solution (an analytical solution for these equations is impossible; therefore, an iterative numerical solution method is used on a mesh to approximate the partial differential equations into of approximate algebraic equations), by advancing the previous solution through time and/or space to obtain a possible description of the whole flow field of interest.

The CFD software analysis takes place in four stages:

First, a preprocessing application (in the present work, *Ansys DesignModeler*) is used to establish the geometry of the model. Second, when the geometry is complete, the boundaries (such walls, inlets, outlets) are named for the specific model in *Ansys Mesh*, and the computational domain is divided into hexagonal or tetrahedral (our case) cells in 3D, which form the mesh.

This mesh is then imported to a commercial Navier-Stokes Solver, *Fluent*, which is a finite volume method (FVM) based code for fluid flow simulations. The *Fluent* (in the present work, v14.5) [33] is a powerful computer program for modeling fluid flow and heat transfer in complicated domains. It provides mesh flexibility and works through flow problems with various geometries.

It is important to notice that proper boundary conditions such as wall temperature, inlet velocity, and gauge pressure are applied in the computational domain. As soon as the solver generates the flow field data at each point, after solving the appropriate governing equations, it is exported to a data processor (in the present work, *CFD-Post*) to analyze the solution through line plots, flow variable contours... This data can also be exported to other software such as Excel to allow comparisons with the other calculations and data in a straightforward manner.

In this chapter, the procedures for these four stages to described in detail. This will include the major impact on the computations (mesh influence, discretization, initial solution, time step influence, boundary conditions, etc.)

5.2 Design Modeler

The model was constructed according to the dimensions used in [34][35]. In order to minimize the computational time of the simulations, the virtual model was built only representing the main parts of the realistic scaled model, with the assumption that the flow pattern will not be affected by “external” components (cables, flow meters, etc.).

The dimensions of the virtual model are $0.75 \times 1.25 \times 0.45 \text{ m}$ (not including the rectangular boxes of the inlet and outlet). The model is visually presented, and the consisting parts are described in Figure 5.1 and Table 5.1. A front view and a top view of the model along with most of the dimensions can be found in Figure 5.2 and Figure 5.3, respectively.

The method to create the geometry of the model, in this thesis, was first to construct the fluid (air) domain; then, by means of the freeze tool, it is possible to configure the other two remaining domains (Slab and Suspended ceiling).

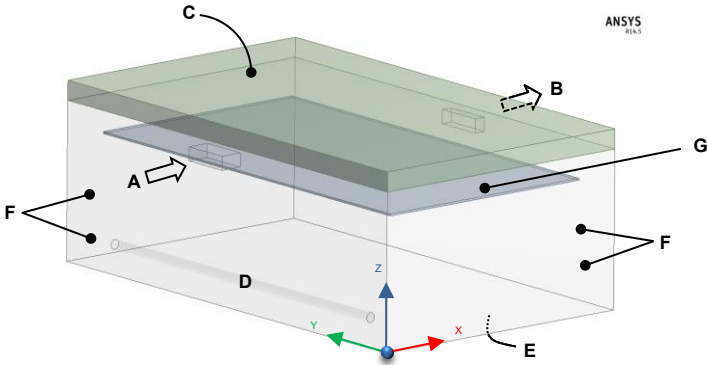


Figure 5.1 – Geometry of CFD model

Table 5.1 - Description of the Figure 5.1

A	Air Inlet
B	Air Outlet
C	Concrete Slab
D	Cylindrical Heat Source ⁹
E	Floor
F	Side Walls
G	Suspended Ceiling

⁹ The heat source is represented as a heat flux in the surface of the fluid, it is misleading to recognize as a body

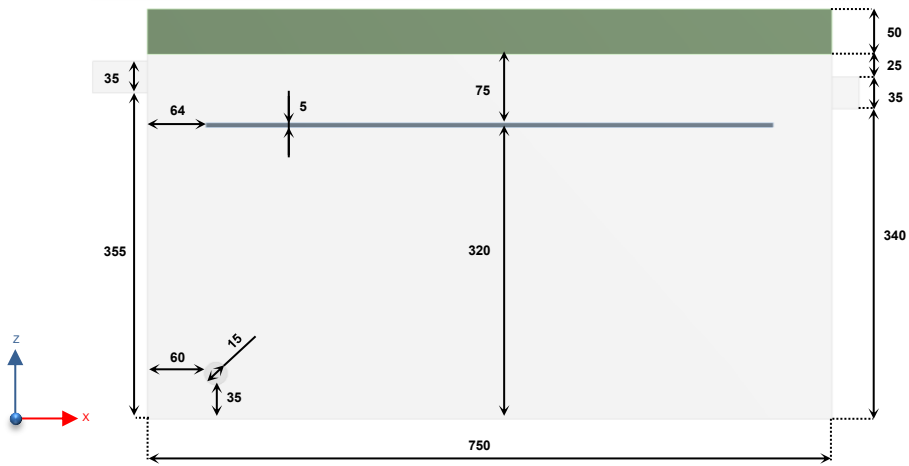


Figure 5.2 - Front view of the CFD geometry model with the corresponding dimensions in millimetres.

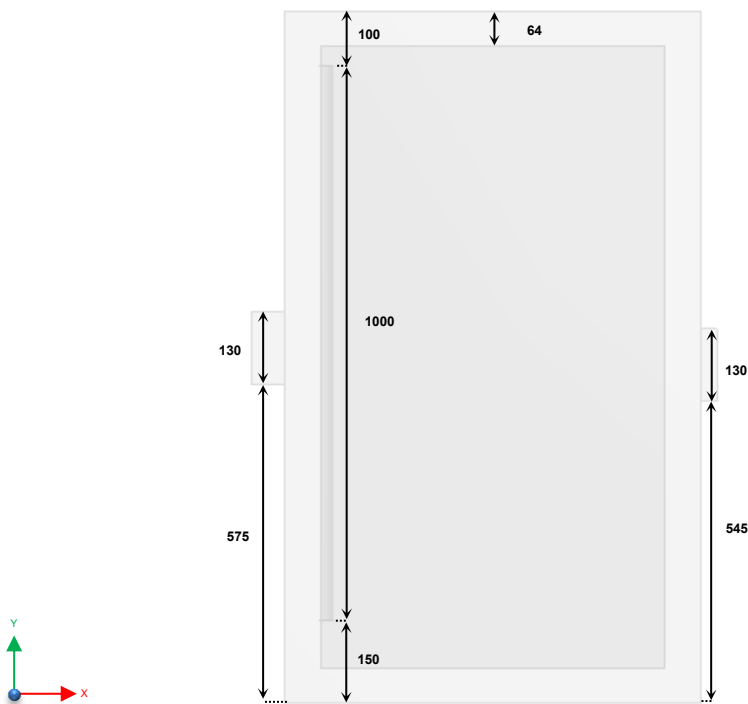


Figure 5.3 - Top view of the CFD geometry model with the corresponding dimensions in millimetres

5.3 Mesh

Mesh generation is one of the most critical aspects of engineering simulation. Too many cells might result in long solver calculation, too few mesh elements are at risk of not having numerically accurate results. ANSYS ICEM was used to build an unstructured mesh that contains solely tetrahedron cells

The principal demand that leads to an unstructured grid choice is given by the need of a better discretization in regions with strong flow variations. In fact, in the case of an unstructured mesh, this can be fulfilled by effortlessly refining in areas where large gradients of solution variable (e.g. velocity or temperature) occur, without adding unnecessary cells all over in the computational domain as normally happens in the structured grid approach. This important unstructured grid advantage has been used in our case to improve the plume area. Consequently, the growth rate was kept close to one, to make the transition, cell to cell, slow.

After some mesh techniques and operations, we start with approximately 200 000 control volumes, mainly assembled by unstructured tetrahedral elements (Fluid) and by a small fraction of hexagonal elements (Slab and Suspended Ceiling). This mesh is represented in Figure 5.4 and Figure 5.5.

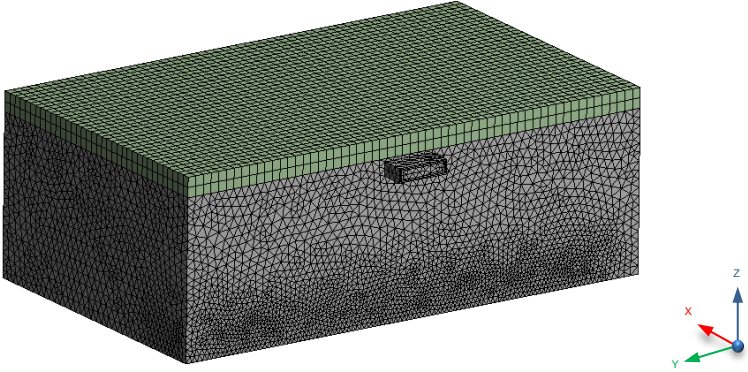


Figure 5.4 - Isometric view of the computational mesh

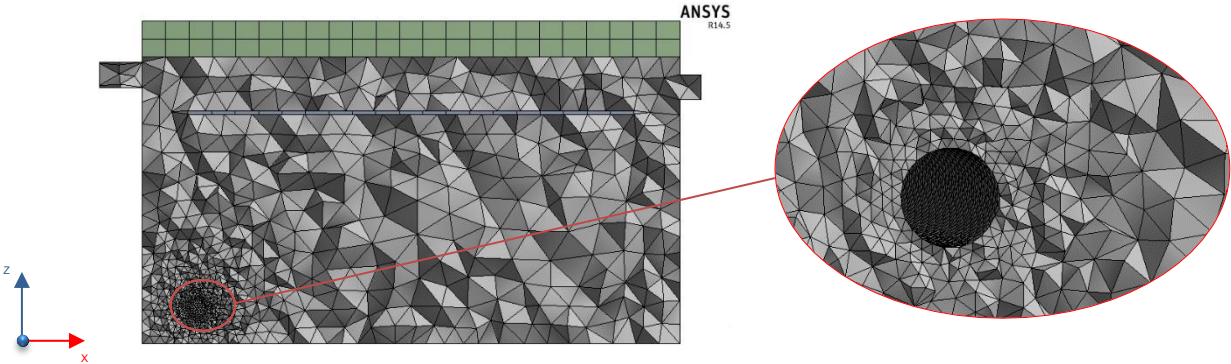


Figure 5.5 - Mesh view in the Plane $Y = 0.625m$, with detailed view on the heat source;

In this section, all boundaries should be named, to make an accessible definition to the solution method for next step (*Fluent Setup*). The inlet, outlet, side walls, floor, outer faces of the concrete slab and the face in the fluid representing the heat source are defined in this step, as in Figure 5.1.

Another main task of the thesis is to optimize the mesh of the model. As we know mesh quality affects significantly the result of the simulation. The smaller the size of mesh element the larger memory space is required, which significantly decreases the speed of calculation and lowers the efficiency of simulation. Therefore, a mesh dependency test is necessary before presenting results produced by CFD, to find whether the numerical modeling shows consistency and efficiency representing the real physics of the fluid flow or not. Details of the mesh dependence test are addressed in the next section.

5.3.1 Mesh Independence Study

The grid independence study is carried out by five sets of mesh densities: Mesh1 (200 000 cells, coarse), Mesh2 (500 000 cells, medium, Figure 5.5), Mesh3 (800 000 cells, fine), Mesh4 (1 100 000 cells, very fine) and Mesh5 (1 700 000, extremely fine). The method of comparison was the temperature at three different points (Figure 5.6), through 12 hours of heating; the dependence of the mass flow (inlet and outlet) and the average room temperature according to the mesh density.

For this study, the boundary conditions are: 50 W of heat load; constant ambient temperature of 23 °C; and the external convection coefficient is $3W/m^2K$ in all the exterior walls. The solver settings, spatial and temporal formulation are described in Table 5.3 and Table 5.4, respectively.

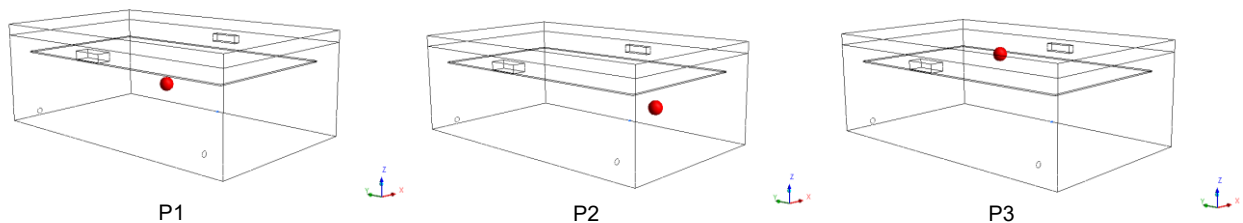


Figure 5.6 - Point 1 (0.375;0.625;0.2) middle of the model, Point 2 (0.375;0.2;0.2) corner of the model, Point 3 (0.375;0.625;0.375) middle of the plenum, respectively

The results of the temperature at the three points are provided in the Figure 5.8, It should be noted that each simulation has 77 time steps¹⁰ (represented as dots in the figure). The number of iterations per time step is that require to achieve Fluent default convergence criterion.

It is also important to highlight, and keep in mind that for each mesh, the physical point compared may not be exactly the same. In fact, the software does not actually give the temperatures at point 1, 2 and 3, but rather the temperature at the grid node of the surrounding cell, as shown in Figure 5.7.

¹⁰ $3 \times 100s + 5 \times 300s + 69 \times 600s$

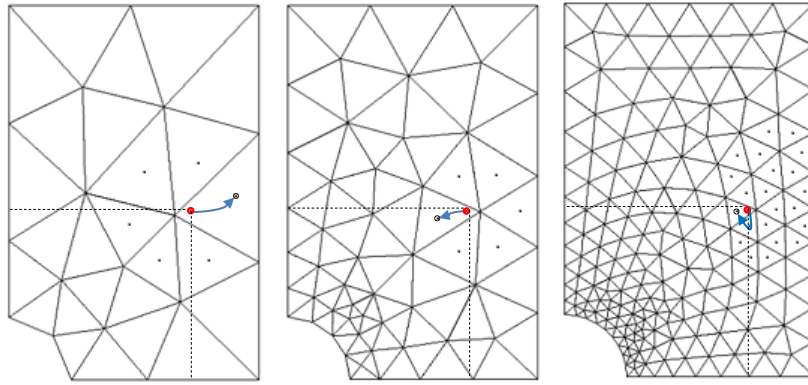
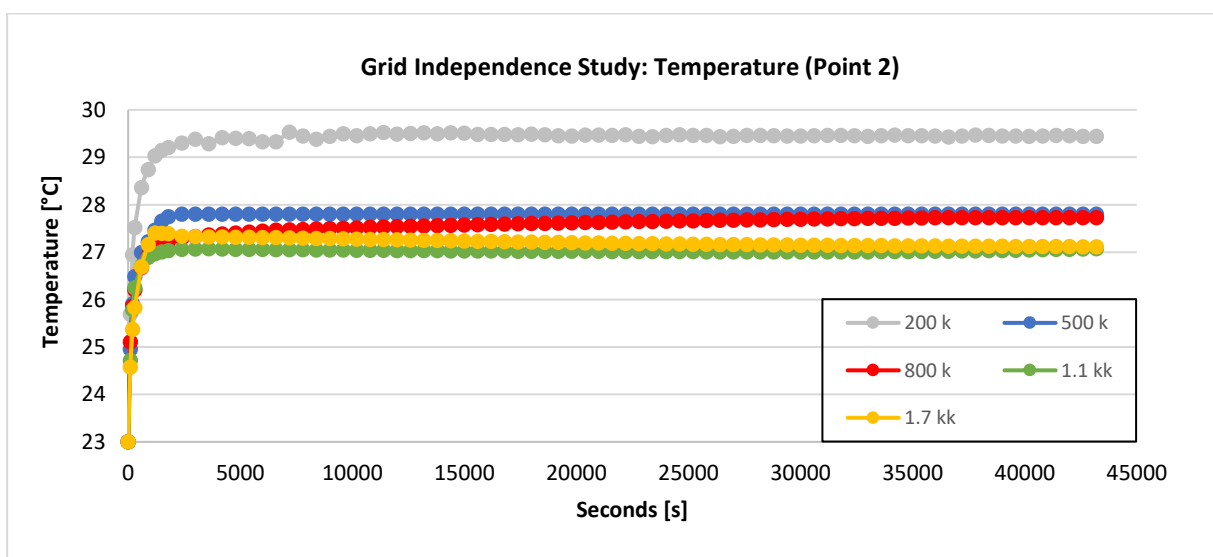
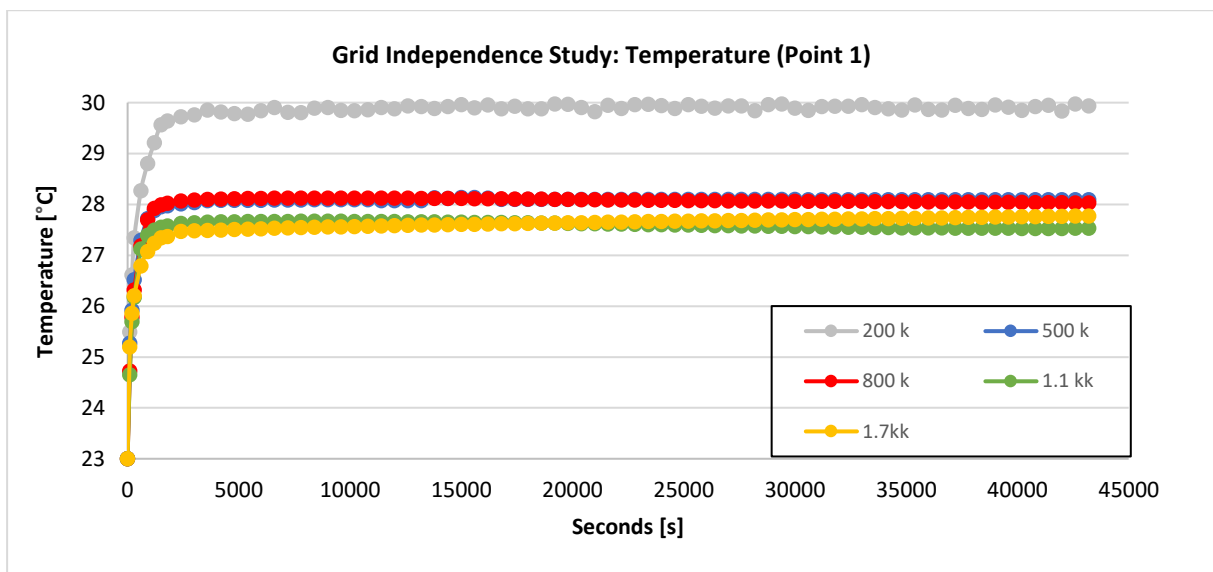


Figure 5.7 - Simplified scheme of computational deviations for the same physical point (Red dot) depending on the size of the mesh; ANSYS FLUENT solver uses finite volumes cell centred



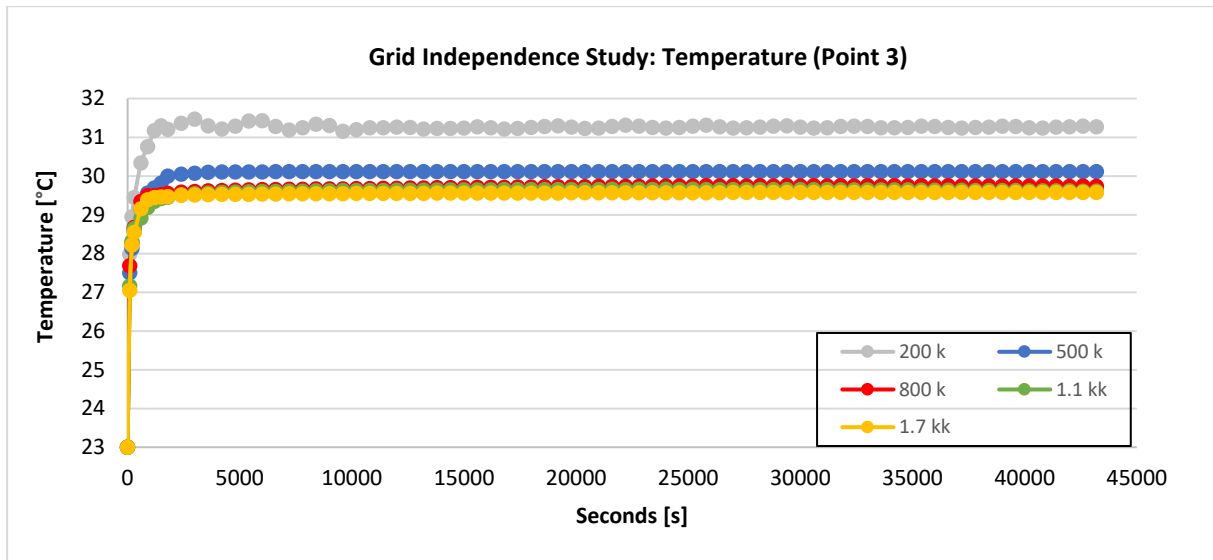


Figure 5.8 - Mesh Size influence - CFD Temperature vs Seconds, in three points. 12 hours of heating period. 1k = 1000

There is a noticeable difference between the temperatures calculated using Mesh1 (200k) and the other meshes, which demonstrates that Mesh1 is not fine enough to accurately resolve the airflow considered in this thesis. The mass flow rate at the openings, and the mean temperature, at the end of the heating period, are provided in the Table 5.2

Table 5.2 - Mesh Size influence, Numerical difference of mass flow rate through the openings and the mean fluid temperature

		Mesh size			
		500 000 cells	800 000 cells	1 100 000 cells	1 700 000 cells
Mass Flow Rate (<i>g/s</i>)	Air Inlets	0.469265	0.429176	0.403058	0.391253
	Air Outlets	0.469716	-0.439707	-0.40291	-0.391451
	Net Results	$-4.5 \cdot 10^{-4}$	$-5.31 \cdot 10^{-4}$	$1.48 \cdot 10^{-4}$	$-1.98 \cdot 10^{-4}$
Mean Temperature (<i>K</i>)		305.731	305.03	304.513	304.391

The mass flow rate through the openings of the numerical model, for three most refined meshes, varies only marginally. There was approximately 6% difference between Mesh3 (0.429176 *g/s*) and Mesh4 (0.403058 *g/s*) and less than 3% difference between Mesh4 and Mesh5 (0.391253 *g/s*).

Regarding the previous results and considering both accuracy and the CPU computing time, Mesh4 with about 1 100 000 cells gave a robust and grid-independent solution. But looking at the mesh, tetrahedral cells does not provide much useful information about its quality. Hence, we need to rely on grid statistics. The orthogonal quality is a measure of the quality of the mesh, ranging between 0-1,

where values close to 0 correspond to low quality and close to 1 correspond to excellent quality. The average orthogonal quality was 0.85 for this mesh. Values between 0.70 and 0.95 are considered to be very good. So, for these reasons the 1 100 000 mesh was used in the remaining simulation runs (the intent of this mesh is not to have the best results but to test the consistency of the scaled model, without being too time-consuming).

For this mesh, 1000 iterations take about 4.5 hours of wall-clock time on an Intel Core i5-6500, 16GB RAM, PC with a nominal CPU speed of 3.2 GHz. For each simulation in *Fluent*, requires 2 GB of computer temporary memory (RAM) and one third of CPU total processor power. The GPU (graphics) is almost useless.

5.4 General Solver Settings

As with all CFD software, there is a large amount of settings available for adjustment in *Fluent* to get the desired simulation and small modifications in the settings can have a large impact on convergence as well as in the results. During the beginning of this project, a lot of focus was put into modifying the settings in order to get a converged solution with residuals at acceptable levels. The level of convergence showed to be very sensitive and highly dependent on the choice of the numerical scheme for pressure-velocity coupling, spatial discretization method and the initial guess of the flow field. A summary of the most relevant settings for the simulations performed during this project can be found in Table 5.3, Table 5.4 and Table 5.5.

The pressure-based solver is used when the flow is incompressible (this solver reduces the time to overall convergence, taking momentum and pressure (or pressure correction) as the primary variables, solving pressure and momentum continuity equations simultaneously [36]). The Coupled solver was selected for all the simulations, as it seemed to offer a more robust convergence trend than the other solution methods. The time formulation is set to Transient.

Under-relaxation factors are used to control the governing equations, stabilizing the convergence behavior of the outer nonlinear iteration. The solution controls used were the default established by the Coupled solution method. In this case, the flow courant number, pressure, and momentum under-relaxation factors were set as 0.9, 0.75, and 0.75 respectively, the others were taken as default.

Table 5.3 - General *Fluent* Solver Settings

ANSYS Fluent	General Settings
Solver Type	Pressure-Based Coupled
Time Dependency	Transient
Viscous	RNG $k - \epsilon$
Wall Function	Standard
Gravity	On

The Body Force Weighted is used due to the conclusion drawn in the previous section (4.3), that the problem is dominated by buoyancy forces. The second-order upwind differencing scheme is used to evaluate the convection terms for the Navier-Stokes equations, the energy equation, and the turbulent transport equation, in order to reduce numerical diffusion and increase solution accuracy, Table 5.4:

Table 5.4 - Spatial and Temporal Formulation

Spatial Discretization	
Gradient	Least Squares Cell Based
Pressure	Body Force Weighted
Momentum	2 nd Order Upwind
Turbulent Kinetic Energy (k)	2 nd Order Upwind
Turbulent Dissipation Rate (ϵ)	2 nd Order Upwind
Energy	2 nd Order Upwind
Under-Relaxation Factors	Default
Temporal Formulation	
1 st Order Implicit	

Providing a good initial guess of the mean flow field, that is close to the final solution, means the solver has to do fewer iterations per time step to reach the converged result. Therefore, reducing simulation time [36]. After some simulations, it was concluded that the initial guess specified in Table 5.5 was the closest solution of the problem.

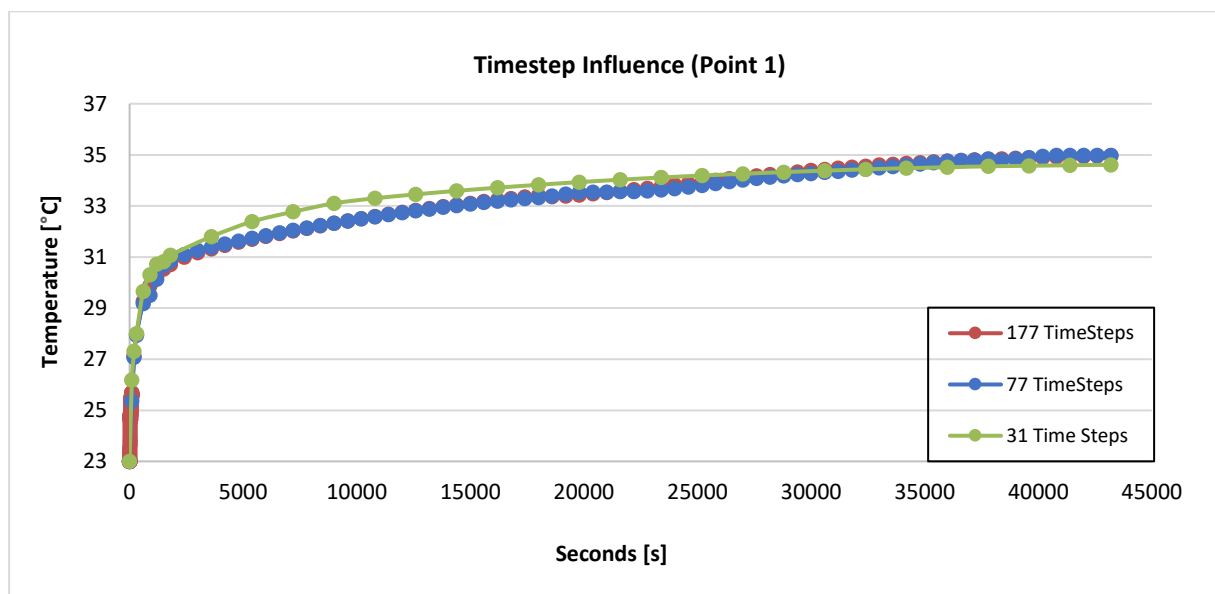
Table 5.5 - Initial Solution Condition

Gauge pressure (Pa)	0
x velocity (m/s)	0.1
y velocity (m/s)	0.1
z velocity (m/s)	0.1
Turbulent kinetic energy (m^2/s^2)	1×10^{-2}
Turbulent dissipation rate (m^2/s^3)	1×10^{-3}
Temperature ($^{\circ}C$)	23

The last step required is one of the most relevant procedures to consider, the time step method. As a starting point, a suitable time step size is estimated as: (derived from CFL number)

$$\Delta t \approx \frac{\text{Typical cell size}}{\text{Characteristic flow velocity}} \approx \frac{50\text{mm}}{10\text{ cm/s}} = 0.5\text{s} \quad (5.1)$$

Figure 5.9 gives a comparison of temperature distribution at point 1, depending on the number of time steps. The approach adopted in the equation (5.1), was represented in the figure as the red line.



11

Figure 5.9 - Red Line: 2x0.5s + 99x1s + 2x100s + 5x300s + 69x600s; Blue Line: 3x100s + 5x300s + 69x600s; Green Line: 3x100s + 5x300s + 23x1800s; Period of heating (12h) with rising ambient temperature

In an effort to minimize the computation time, the stepping method of the blue line was selected for the next simulations.

Solution process control was verified by ensuring that the residual curves (for each equation) reaches the *Fluent's* default convergence criteria. This specified tolerance gives an acceptable accuracy. Residual plot of the chosen stepping method is shown in Figure 5.10.

¹¹ The other points previously presented behave similarly

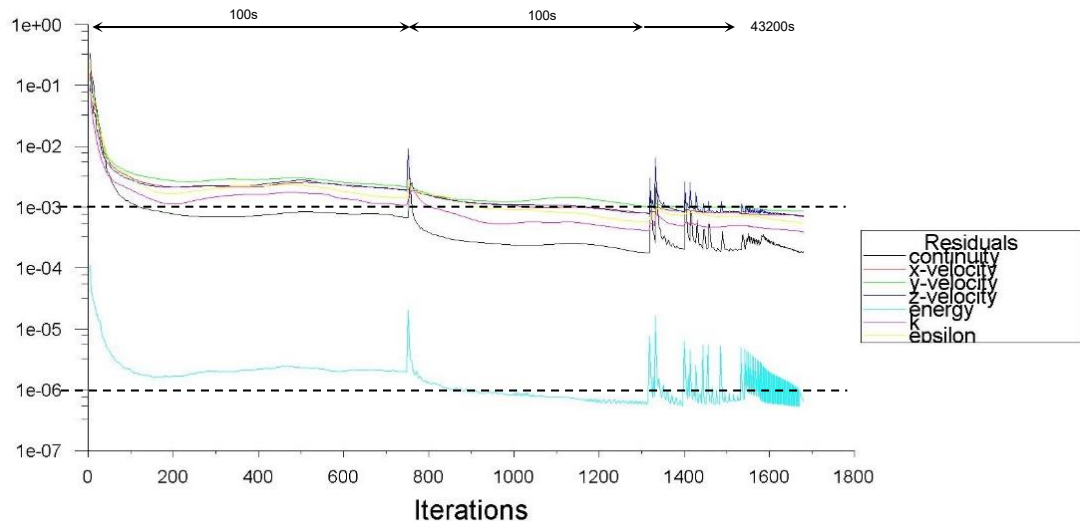


Figure 5.10 - CFD Simulation Residuals, Stepping Method of the Figure 5.9 (blue line)

This process lasts approximately 1,700 iterations, where the jumps in residuals correspond to the transition of each time step of the solution. It was noticed that the first time-step, had difficulty converging to the specified value (closest values, $1\sim 2 \times 10^{-3}$). This is not a big issue because comparing the stepping method of the red line, all the time-steps converged, and the solution wasn't so different. After the second time-step, the solution appears to converge rapidly only after some iterations.

5.4.1 Boundary conditions (BC)

The boundary conditions for the simulations are selected cautiously in order to describe appropriately the physical conditions. *ANSYS Fluent* allows a wide range of boundary conditions that permit the flow to enter and exit the solution domain. In this work, 3 types of boundary conditions were chosen: velocity-inlet boundary, pressure-outlet boundary and wall boundary. In Figure 5.1 one can see where the boundary condition is implemented and in Table 5.6, the boundary type along with the thermal condition is defined in each boundary region.

Table 5.6 - Boundary Conditions set up

	Type of BC for Momentum Equations Daytime / Nighttime	Type of BC for Energy Equation Daytime / Nighttime
<i>Air Inlet</i>	Pressure Outlet / Prescribed velocity	Sinusoidal temperature
<i>Air Outlet</i>	Pressure Outlet	Sinusoidal temperature
<i>Concrete Slab</i>	Law of the wall	Convection (& Radiation)
<i>Cylindrical Heat Source</i>	Law of the wall	Heat Flux / Adiabatic
<i>Floor</i>	Law of the wall	Convection (& Radiation)
<i>Side Walls</i>	Law of the wall	Convection (& Radiation)

The “pressure outlet” was chosen (with gauge pressure taken equal to zero). This boundary condition is used to define the static pressure at the flow outlets. In this case, backflow total temperature is taken equal to outdoor temperature (for more realistic simulation). User Defined Function (UDF) is used to achieve this specific ambient boundary temperature condition. Compiling the C program as shown in Appendix 1, this specified temperature function keeps the boundaries simulating the typical temperatures of the day, which varies approximately as a sinusoidal function. It is important to define this temperature not only for the air supply during night (forced) ventilation but also during the day since the supply and extraction slots remain open. During the cooling process, the velocity-inlet boundary condition was chosen in order to define constant velocity of 8 m/s at the inlet boundary (Figure 5.1 - A).

The “wall” boundary condition was chosen to represent all the remaining BC and is used to define the fluid-solid interface. In this option, for viscous flows, the no-slip boundary condition is enforced at the wall and defined as stationary. The heat source (Figure 5.1 – D), will be emitting 50 W which is equivalent

in this case to 629 W/m^2 . The remaining external walls (Figure 5.1 – C, E, F), were defined considering losses by convection and radiation, according to the properties and thickness of a virtual wall (it was not modelled). Table 5.7 lists the characteristics of the various types of materials used in these simulations.

Table 5.7 - Properties of the materials used in the simulations; Specified thickness for the walls of concrete and XPS

<i>Materials</i>	Air	Concrete [37]	XPS [38]	Cardboard
<i>Properties</i>	[30][31]	(50 mm)	(40 mm)	[39]
<i>Density (kg/m^3)</i>	1.22	2200	30	130
<i>Specific heat (J/Kg.K)</i>	1006.43	880	1220	1700
<i>Thermal conductivity (W/m.k)</i>	0.0242	1.4	0.034	0.35
<i>Emissivity (ϵ)</i>	0	0.85	0.9	0.81
<i>Viscosity ($\text{N.s/(m}^2\text{)}$)</i>	1.7894×10^{-5}	-	-	-
<i>Thermal expansion</i>	0.00333	-	-	-
<i>Boundary Region</i>	Fluid	Slab	Side Walls, Floor	Suspended Ceiling

6 Simulation Results and Analysis

6.1 Introduction

The results and the discussion are presented in this chapter. Simulations were carried out based on the concepts and methodologies (computational parameters - turbulence model, grid size, boundary conditions, etc.) described in the previous chapters. These simulations are categorized by two types of ventilation: buoyancy-driven (daytime) and mechanical driven flows (nighttime).

CFD analysis will be performed, firstly, for buoyancy-driven ventilation (with high-level openings) and in the next section, as a first stage, the pre-computational results using the established theoretical boundary conditions (radiation involved), will be compared with some unpublished experimental results obtained by Miguel Lança. A simulation without any radiation model will be presented in order to compare the effect of this parameter on the simulations results. Temperature is the property of comparison, especially during the heating period (intense radiation due to the cylindrical source). Subsequently, the impact of the night cooling period (mechanical driven flow) will be also studied.

Finally, the ultimate goal is to evaluate the influence of changing several types of suspended ceiling, in order to improve the performance in lowering ambient temperatures during the working period. The parameters changed were the gap between the suspended ceiling and the room walls.

6.2 Heating Period

In an attempt to obtain the computational results as closest as possible to the experimental values (normal losses due to infiltrations and other irregularities), computational heat losses through the boundaries will be adjusted according to the experimental data, in order to avoid extra heating which leads to higher average temperatures (Figure 5.9, $T_{av,final} \sim 35^{\circ}C$). And by changing the values of the section 4.4-External Boundary Conditions, one can adapt these coefficients and examine their impact on the heat flux.

Thermal resistance given by the equation (4.38) can be studied for the two types of walls.

For the horizontal wall of concrete (Slab), (Table 5.7, thickness-50mm) the thermal resistance is:

$$\frac{1}{A} \left(\frac{1}{h_1} + \frac{L}{\lambda} + \frac{1}{h_2} \right) = \frac{1}{A} \left(\frac{1}{h_1} + \frac{0.05}{1.4} + \frac{1}{3} \right) = \frac{1}{A} \left(\frac{1}{h_1} + 0.0357 + 0.3 \right) \quad (6.1)$$

The convective heat transfer on the inner room surface (h_1) is affected by the indoor air temperature distribution and the near-surface velocities, both of which can vary depending on the air flow pattern in the room. But, taking into account that h_1 is computed by the CFD code, we can only manually change the external convection coefficient. As described in equation (6.1), h_2 has an influence (theoretically) on the heat flux. Figure 6.1 shows the difference for two different convection coefficients, 3 and 12 (reasonable values). Giving a variation in the maximum temperature of $2.2^{\circ}C$ at the point 3, $0.67^{\circ}C$ at

point 1, and 0.35 °C at the point 2. A disadvantage of this method is that the difference of 2.2 °C is not reflected on the other points.

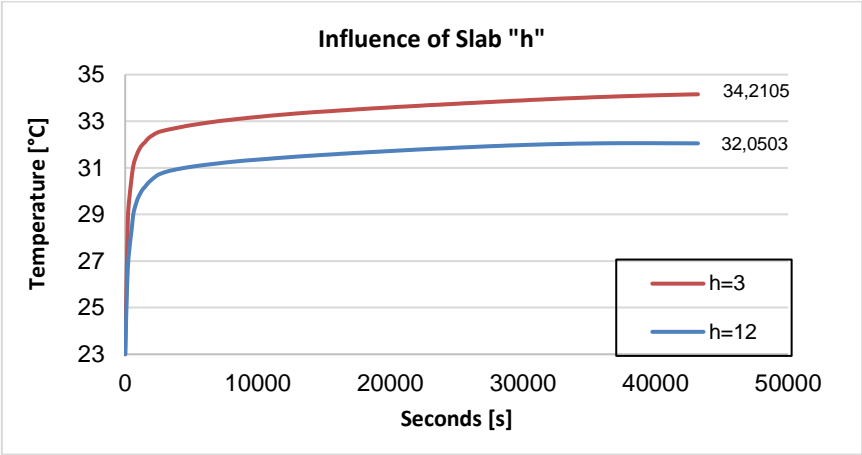


Figure 6.1 - Influence of the convection coefficient at the exterior face of the slab on the temperature at point 3, through the heating period (50W); The convection coefficient of the other wall remained equal to 3 W/m²K.

For the vertical walls of XPS (Table 5.7, thickness-40mm) the thermal resistance can be calculated as:

$$\frac{1}{A} \left(\frac{1}{h_1} + \frac{0.04}{0.034} + \frac{1}{3} \right) = \frac{1}{A} \left(\frac{1}{h_1} + 1.18 + 0.33 \right) \tag{6.2}$$

From the previous equation, it is obvious that the heat flux through walls of XPS is dominated by the conduction resistance. This can be confirmed in Figure 6.2, (h₂ = 3; 8; 12 W/m²K).

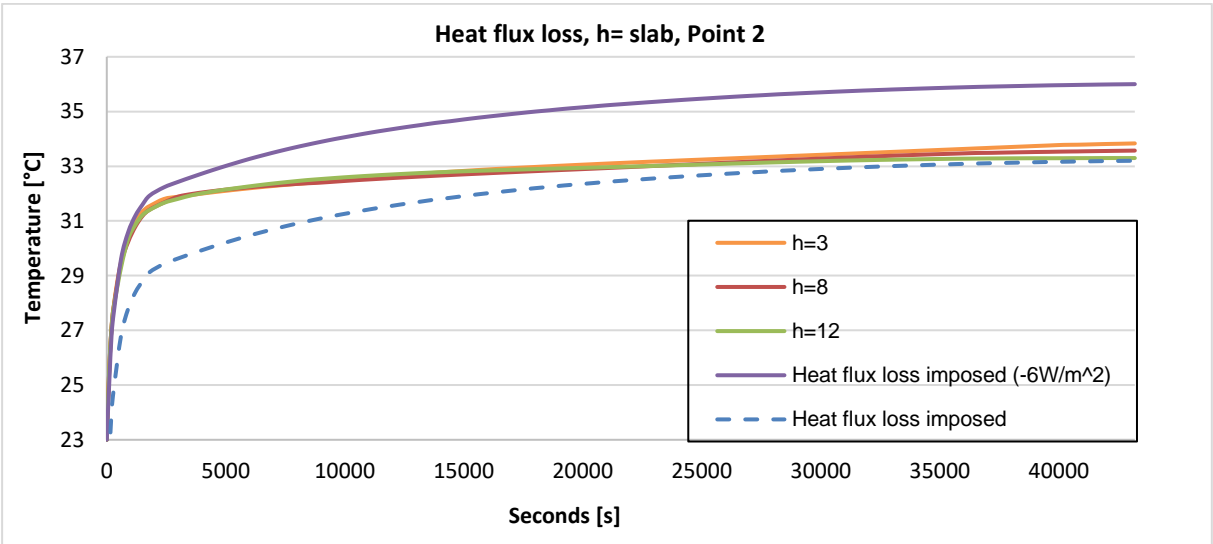


Figure 6.2 - Temperature in point 2, according to the thermal boundary condition (heat flux and convection coefficient) on the side walls and floor. Concerning the heat flux imposed only one simulation was performed; The dashed blue line is a virtual simulation with the same slope of the dashed purple, with the purpose of showing its initial behaviour.

Taking into account these results, one can state that the convection coefficients on the outer side walls and in the floor (in the slab the coefficient remained constant $h = 4W/mK$) shows only a slightly influence on the heat flux loss. So, it was concluded that the use of convection as a thermal boundary condition wasn't an appropriate solution to match the experimental results.

Another option is to establish a constant heat flux loss through the heating period, also represented in Figure 6.2 (dashed simulations). Between 0-20 000s, the effect of a constant heat flux loss is visible, the model is losing the same amount of energy regardless of the interior and exterior temperatures. While with the convection coefficients this loss is gradual and dependent on the working conditions. But, comparing experimental (see Figure 6.3) data with the results of the Figure 6.2, it is interesting how they behave similarly with the dashed simulation run.

It is not our goal to explain the differences between the CFD calculations and the measurements, but the disagreement can be explained by the following reasons:

- Air velocity in the laboratory may not be stagnant inducing flow patterns above the model making low/high pressure regions which could consequently cause higher effective ventilation flow rate than the CFD modeling, resulting in a relatively lower temperature in the experimental model.
- The disagreement could also be due to infiltration in the model during the experiments especially air leakage through cable holes to acquire data and wall edges. The air leakage and infiltration results in extra heat loss which is not considered in the CFD calculation.
- Imperfections on the physical materials (uncertainty in the thermal properties of the construction materials, concrete, and XPS).

For these reasons, it is acceptable to use in next simulation runs a constant heat flux loss, and to find the value that fits the experimental values, we must rely on trial and error, which brought us to the value of $-7.9 W/m^2$ (Side Walls and Floor). As observed from the Figure 6.3 and Figure 6.4, the experimental and the numerical simulation results show evidence of a good agreement. In last two hours of the heating period, the experimental temperature rises faster than the predicted one, this could be explained by unknown experimental events, because it seems that the experimental data does not have any relation with the variation of laboratory temperature. For instance, in Appendix 2 we can see that the maximum CFD Lab Temperature reflects on the CFD Temperature after around 40minutes.

In Figure 6.5 to Figure 6.7 results of temperature and velocity (modelled with radiation), through the heating period can be seen. The results, show the general behavior of hot air. It rises very hot from the heat source creating an uprising thermal plume that attaches to the ceiling and spreads to the opposite side of the model from where it finally falls down attached to the wall into the bottom part of the indoor space, setting a peripheral rotational motion and some vortexes that enhance heat transfer through the enclosure. Nevertheless, as the indoor air is mixed the values of temperature show rising progression both at the upper and the bottom part of the space, and the stratification is shown clearly in the shaded contour plots being the upper buoyant layer above the suspended ceiling the warmest (desired for thermal comfort). In this region the slab is acting as a heat accumulator, with its overall temperature

increasing with time and, as it can be seen through the temperature gradient, the hottest region is on the lower surface of the slab above the heat load. Also in this region, some of the warm air of the plume exits through the left opening (closest) and cold air enters through the opposite opening with the same flow rate.

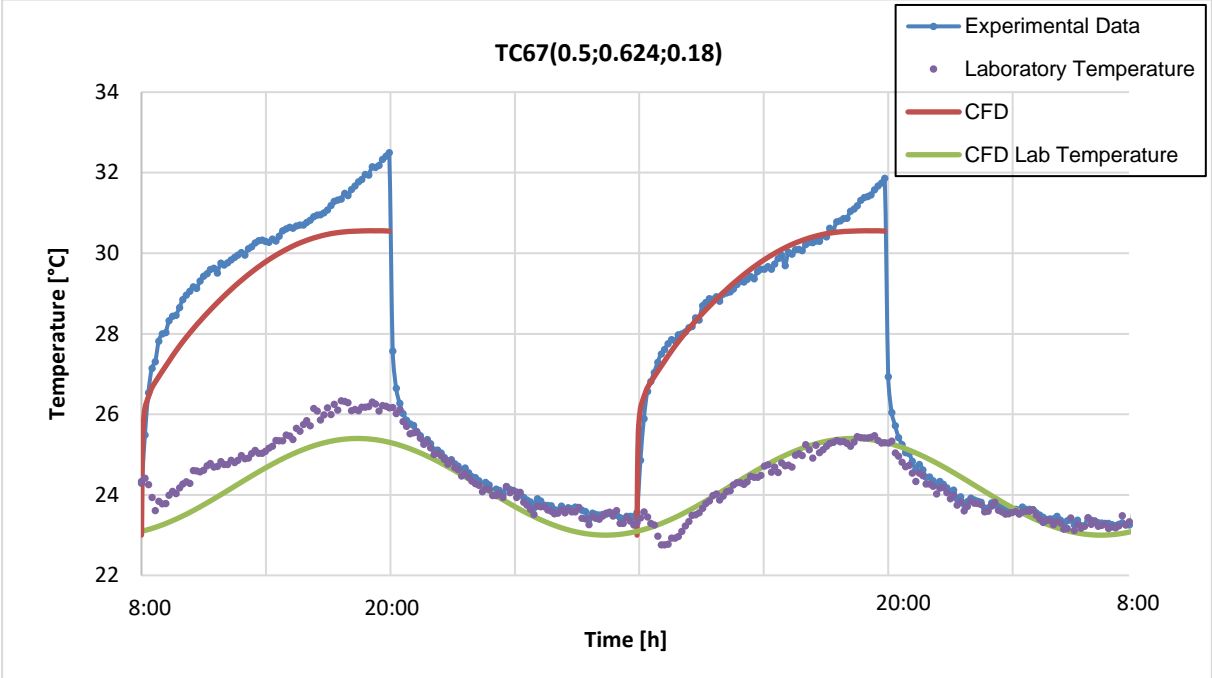


Figure 6.3 - Difference between the measured and calculated temperature in the heating period at thermocouple 35 (plenum) for two days.

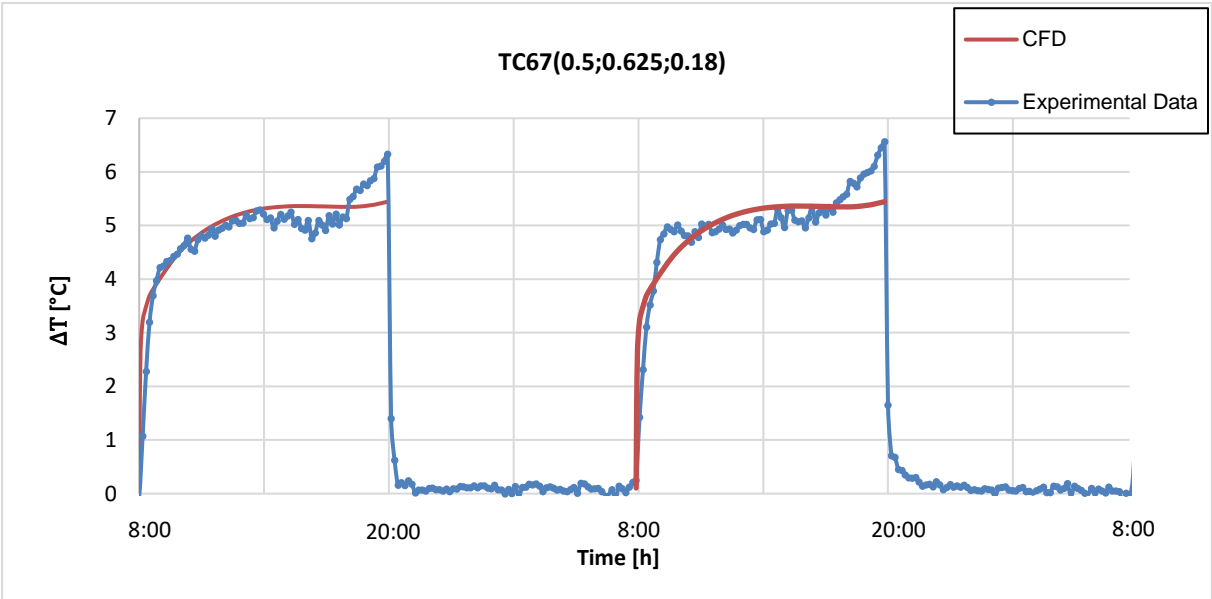


Figure 6.4 - Temperature difference, $\Delta T = T_{measured/CFD} - T_{Lab}$, for two days.

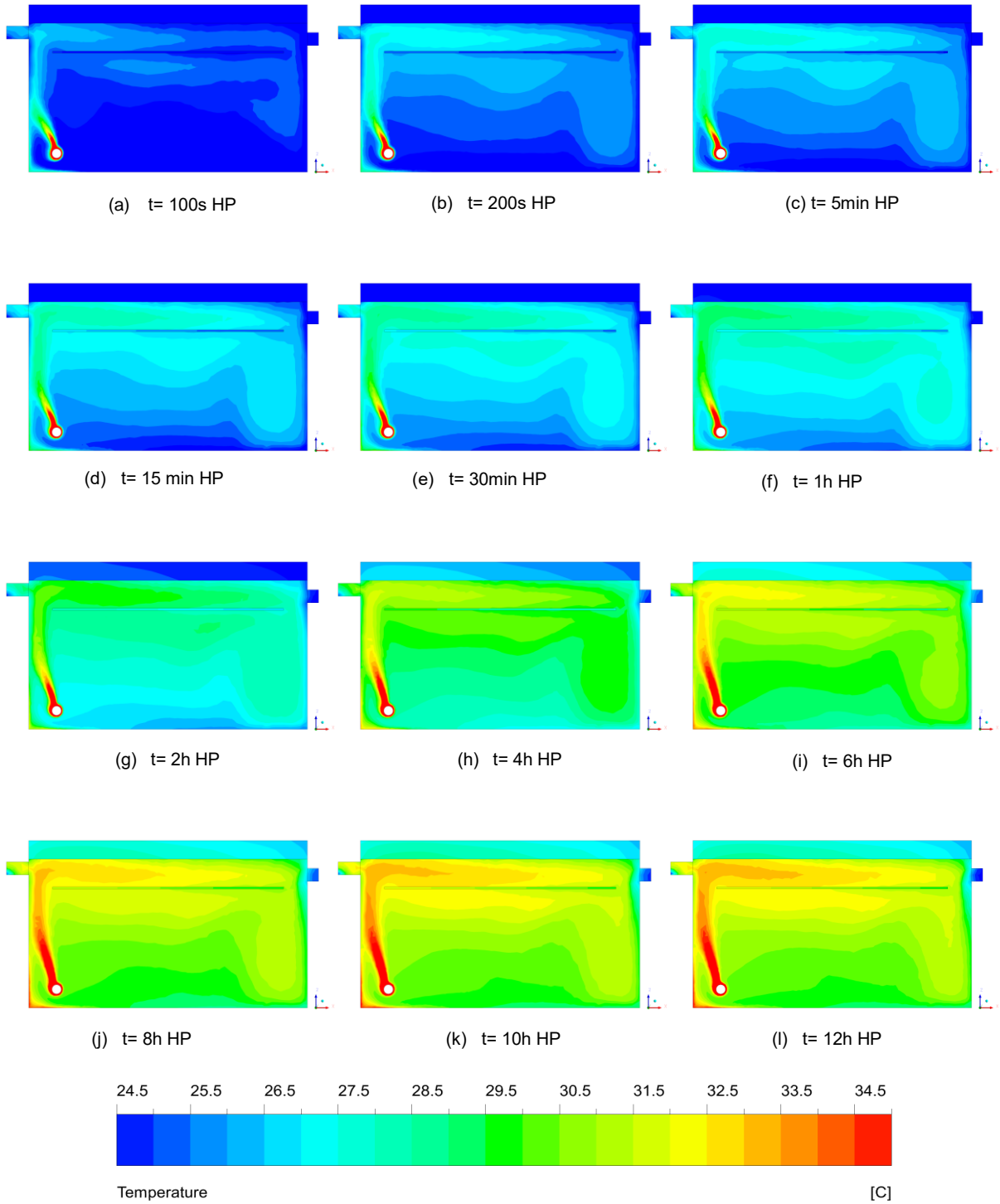
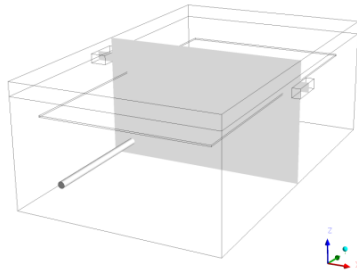


Figure 6.5 - Temperature contour profiles with radiation for twelve heating periods. Plane $Y=0.625\text{m}$. HP - Heating Period

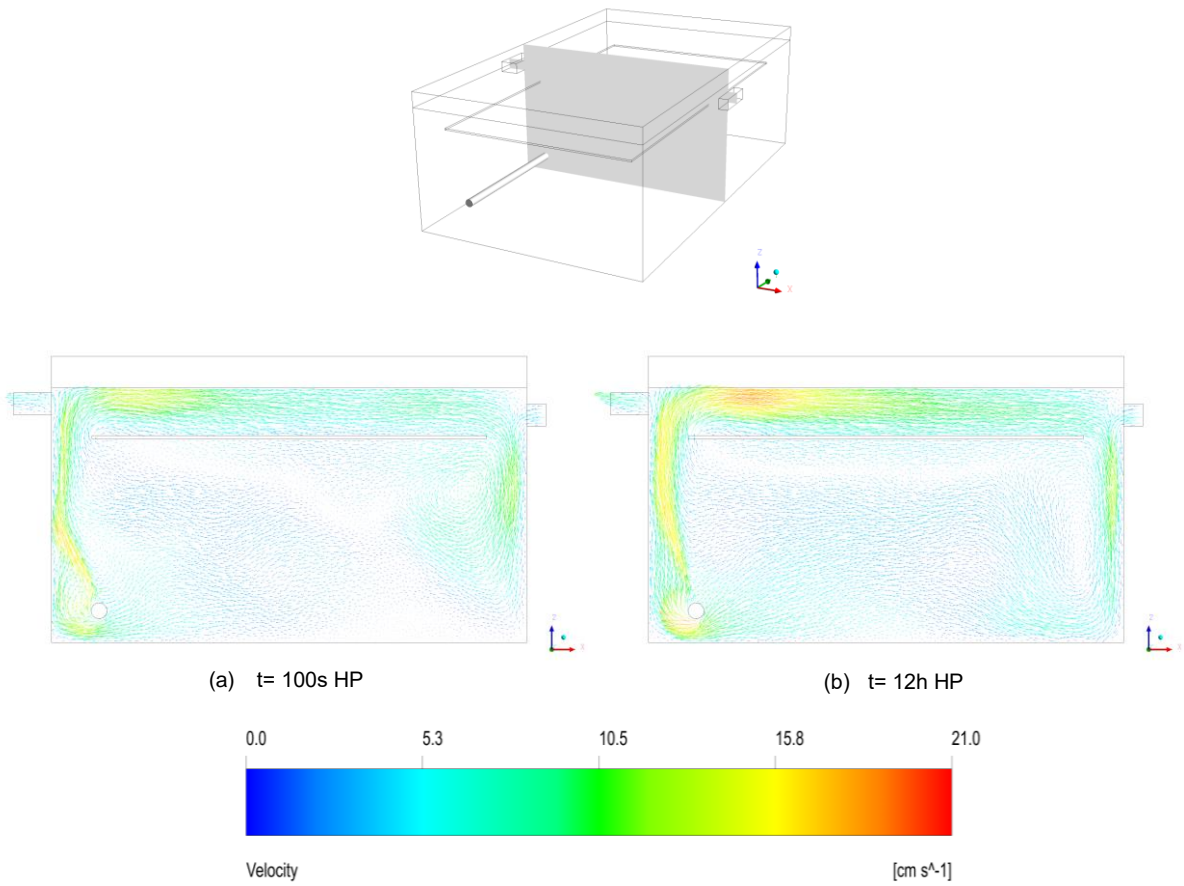


Figure 6.6 - Vector distribution with radiation for two heating periods. Plane $Y=0.625\text{m}$.

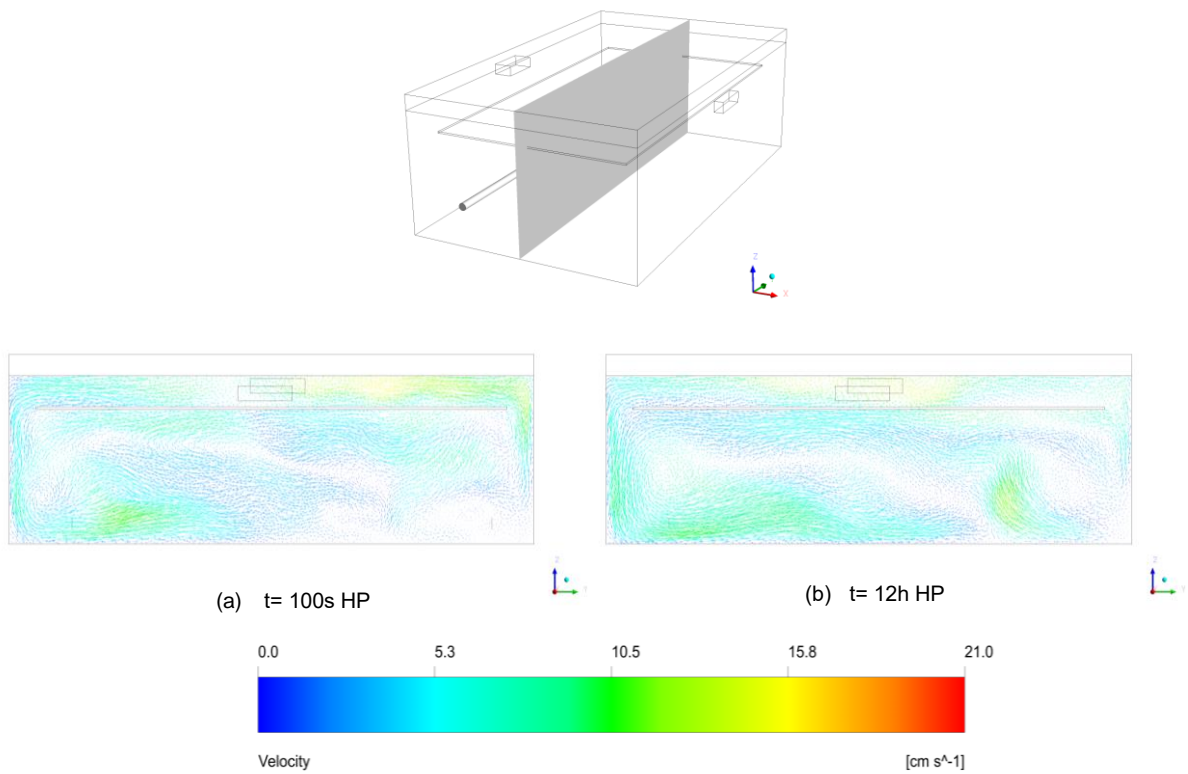


Figure 6.7 - Vector distribution with radiation for two heating periods. Plane $X=0.375\text{m}$.

In order to evaluate the impact of modelling radiation, a comparison is presented in Figure 6.8 in the form of temperature distribution at the end of one heating period. The two simulations were made with exactly the same parameters (except, obviously, the radiation model) and shown on the same scale, although, contrary to what may be intuition, the simulation with radiation is the one who has lower average temperatures (Figure 6.8-(a)). They can be distinguished primarily by the lower left corner.

These differences can be explained by the way the solver emits the heat flux through the cylindrical heat load. In the case with radiation there is an emission of 50 Watts distributed by through two mechanisms, convection to the fluid and radiation to the walls (non-participating medium, S2S model), in other words, a fraction of the power is emitted by radiation and the other by convection (e.g. 20W by radiation and 30W by convection). While in the simulation without radiation, all the power is transferred to the fluid by convection. That's why the temperatures are relatively higher in this latter, and as a consequence, the buoyancy driven ventilation is stronger, causing different air flow rates through the slots (w/o 0.38 g/s, w/ 0.30 g/s) but the same pattern of recirculation is reported.

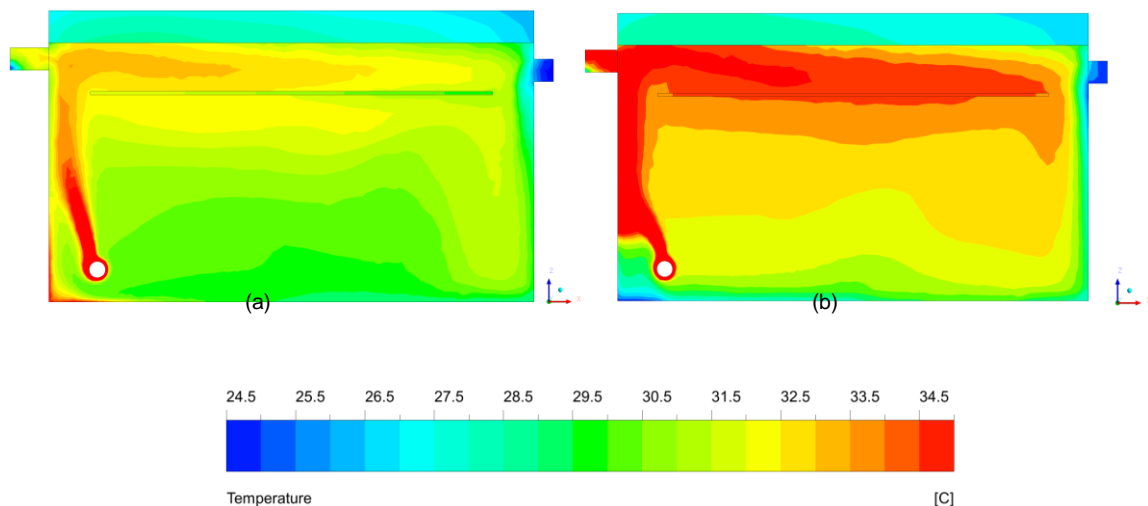


Figure 6.8 - Influence of radiation in the temperature distribution in the end of the heating period (12h); (a)- Simulation with Radiation; (b)-Simulation without radiation. Plane Y=0.625m

6.3 Cooling Period

The following analysis is mainly focused on the night time ventilation. As previously described, the operation is to apply an insufflation velocity of 8 m/s or constant air flow rate (44.4 g/s) through 12 hours. This process is done by advancing the previous heating state with radiation involved. The results¹² of this technique at 12 cooling periods are presented from Figure 6.9 to Figure 6.12.

¹² A smaller stepping method was used :30x60s + 69x 600s

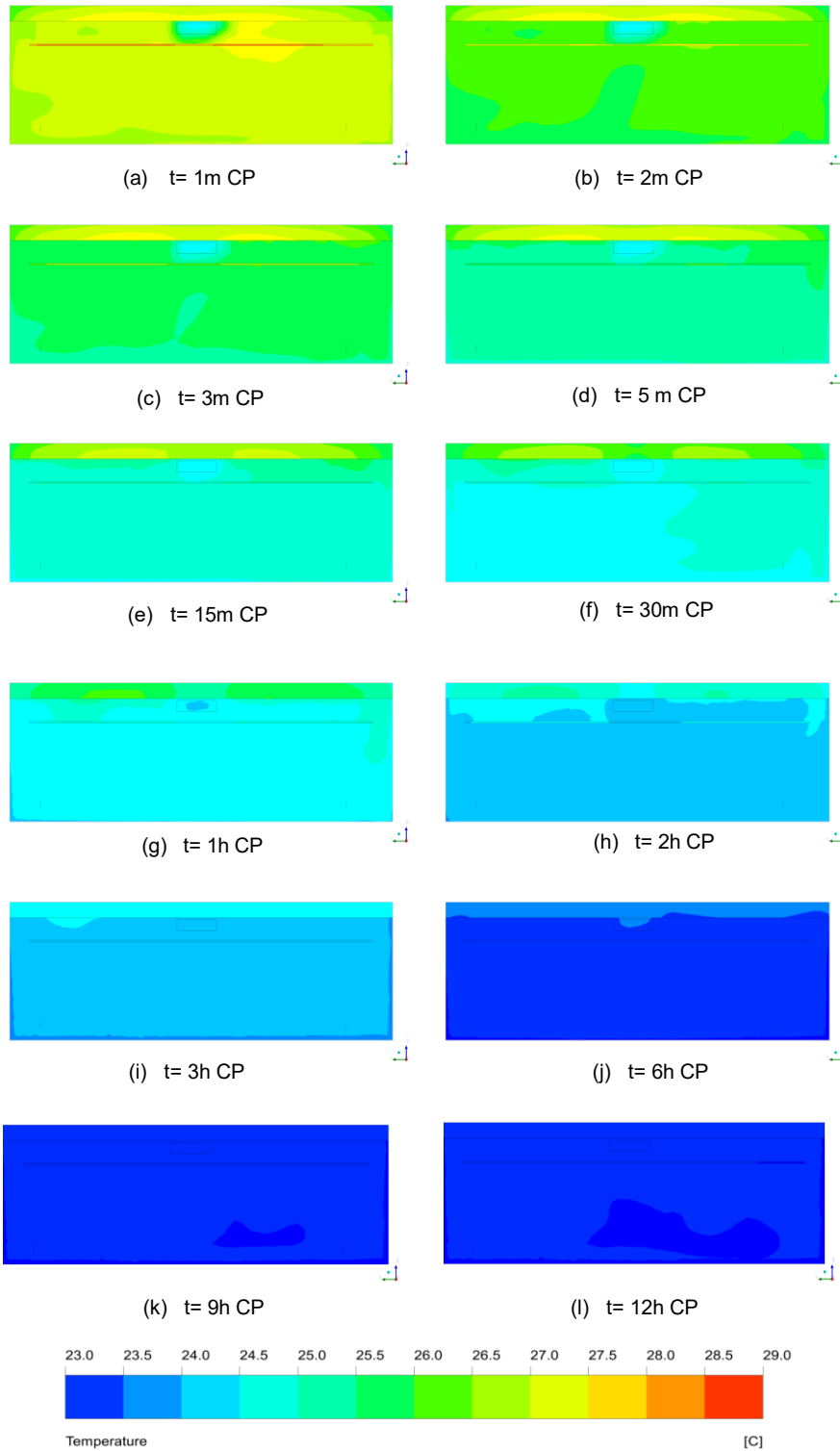
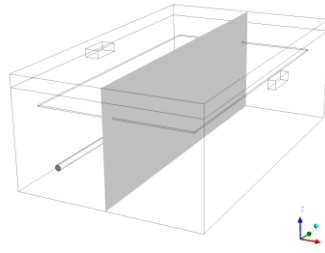


Figure 6.9 - Temperature contour profiles with radiation for twelve cooling periods. Plane $X=0.375\text{m}$. CP - Cooling Period

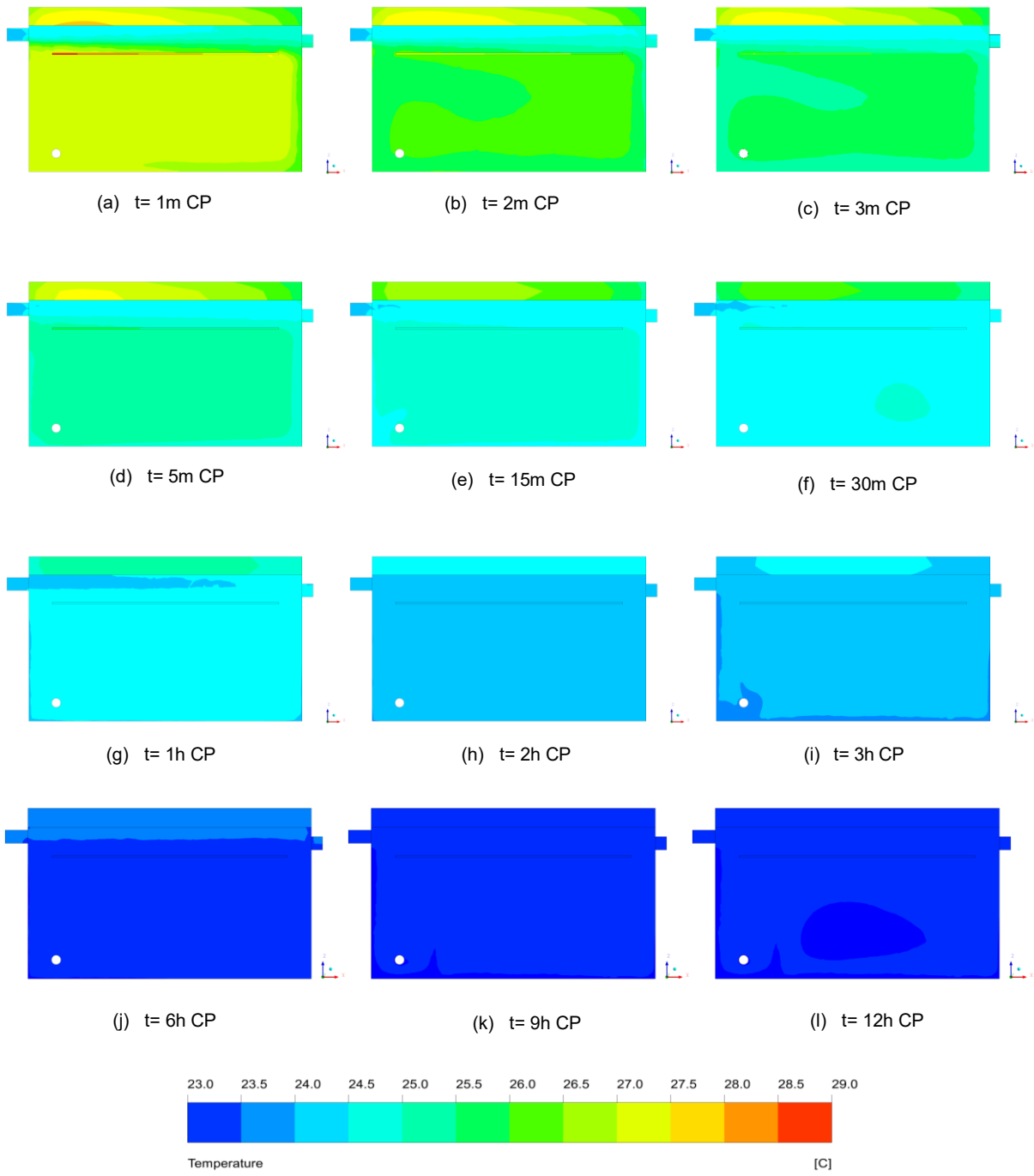
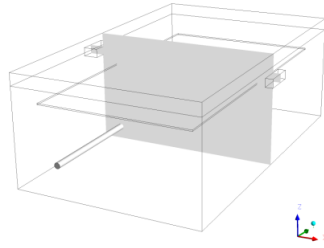


Figure 6.10 - Temperature contour profiles with radiation for twelve cooling periods. Plane $Y=0.625\text{m}$.

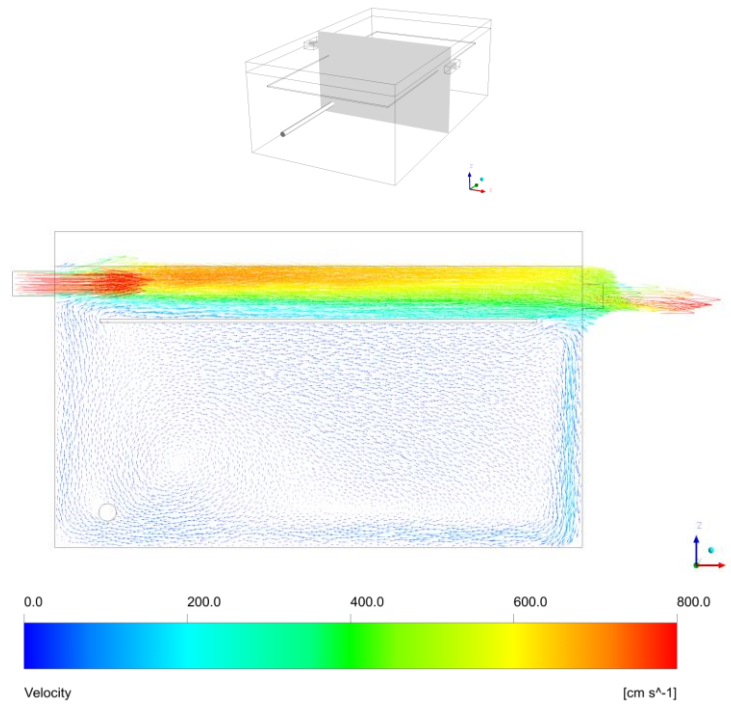


Figure 6.11 - Velocity vector for 60s of operation time (the average velocity in the occupation zone is 50cm/s). Plane Y=0.625m.

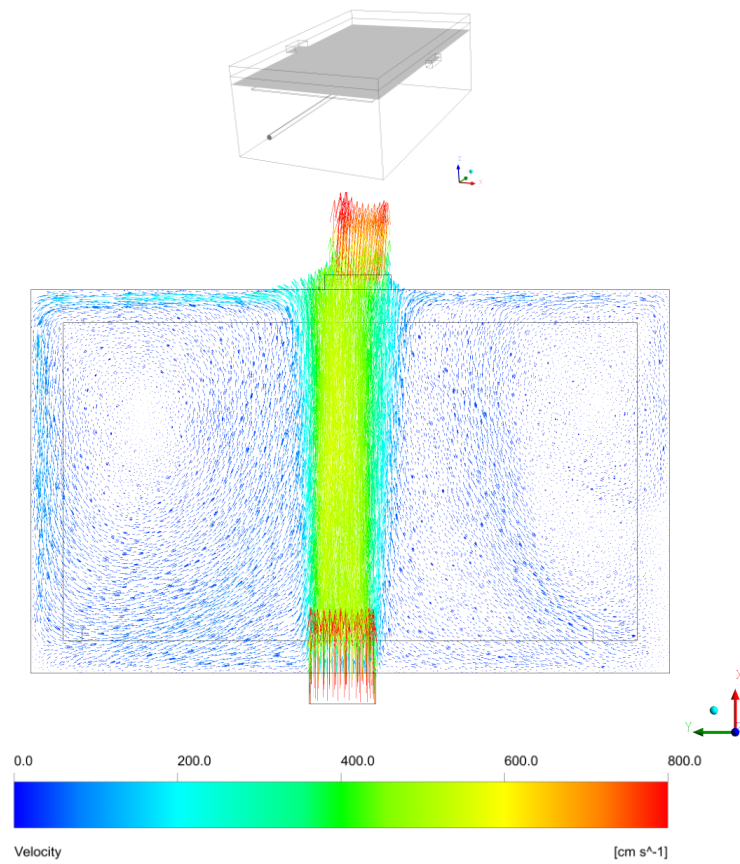


Figure 6.12 - Velocity vector for 60s of operation time, Plane Z=0.361m (plenum).

As it is possible to observe by analysing the temperature contours in two planes, the use of thermal air mass to remove the absorbed heat from space is very effective. It takes less than 9 hours, after the start of process, to uniformize the air temperature. This effect can be explained by the highly transient process of replacing the air within the space with cool ambient air. This exchange it's done through the gaps of the suspended ceiling, Figure 6.11.

Also, in Figure 6.11 and Figure 6.12, it is possible to see the highly transient velocities¹³ in the plenum causing high heat transfer rates with the pre-heated slab. As a consequence, the slab core temperature (Figure 6.13) drops 4.5 degrees in only 6 hours while in the heating period the same difference takes almost 12 hours.

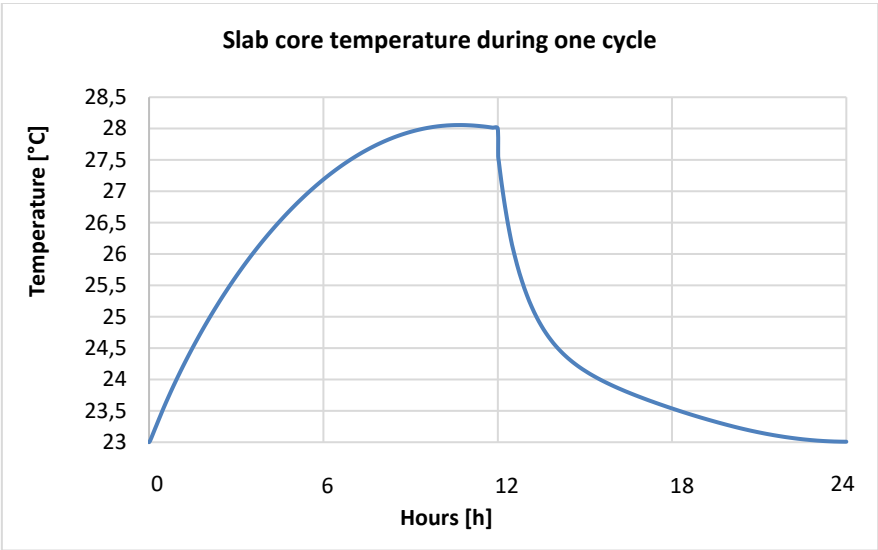


Figure 6.13 - CFD temperature in slab core (0.375; 0.625; 0.425) during one cycle (HP and CP)

One of the advantages of the use of the suspended ceiling during night cooling is that the air velocities in the occupation zone can be low (desired for offices) compared with the case of night cooling without suspended ceiling. These velocities are dependent on the suspended ceiling gaps.

In general, the results illustrate that this technique is very effective, suggesting that the model is ready for another cycle.

¹³ The size of the velocity vectors was increased for viewing purposes

6.4 Suspended Ceiling Influence, HP

In this section we present and analyse the results corresponding to the several design scenarios. This was done with a goal of observing the influence of the gaps on the temperature and mass flow rate through the slots. Four different vertical temperature profiles retrieved from the simulations are drawn in Figure 6.15 and Figure 6.16 for all the desired scenarios ($32 \times 32 \text{ mm}$, $64 \times 64 \text{ mm}$, $90 \times 125 \text{ mm}$, $240 \times 120 \text{ mm}$, W/o) and for two heating periods – 5 minutes and 12 hours. For the sake of better visualization, the locations of the suspended ceiling and the slab are represented by black dashed lines. The location of the vertical lines (from the floor to the outer wall of the slab) is shown in Figure 6.14 and each line has 100 measuring points. It is important to highlight that all the simulations were performed with exactly the same boundary conditions, such as those of the Figure 6.3.

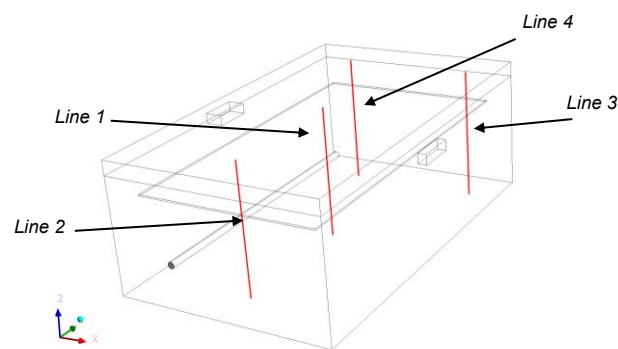


Figure 6.14 – Location of the vertical measurement lines. Line 1 (0.375; 0.625; 0 : 0.45) Line 2 (0.375; 0.15; 0 : 0.45) Line 3 (0.65; 1.1; 0 : 0.45) Line 4 (0.2; 1.1; 0 : 0.45)

In Figure 6.15 and Figure 6.16 we can see that the temperatures calculated below the suspended ceiling (representing the occupation zone), are higher in the scenario with smaller peripheral gap - Red line. This is easily explained by analysing the mass flow rate through the inlet/outlet slot, Table 6.1. Here we see that the values for the two periods are relatively low compared to the other scenarios, which means that the suspended ceiling is restricting the mass flow rate through the peripheral gaps and working as an insulator between the two spaces keeping away the desirable heat exchange between the slab and thermal plume. For the case without suspended ceiling relatively high temperatures are registered, as well, in the occupation zone. Surprisingly, these two configurations are frequently encountered in buildings. Finally, for the remaining scenarios, it is possible to observe, by analysing the graphics that good results are provided in the occupation zone. This shows that, specially for the wider gaps ($90 \times 125 \text{ mm}$, $240 \times 120 \text{ mm}$), there is a temperature homogenization in this zone due to the fact the higher temperature stratification level is now above the suspended ceiling (the opposite occurs in the scenario with a gap of $32 \times 32 \text{ mm}$) and greater heat exchanges may occur with the slab. It is important to highlight that the property value of conduction of the suspended ceiling plays an important role in this homogenization. These facts become more obvious if we look at the temperature contours for the different design scenarios in two heating periods - 5m and 12h, Figure 6.17.

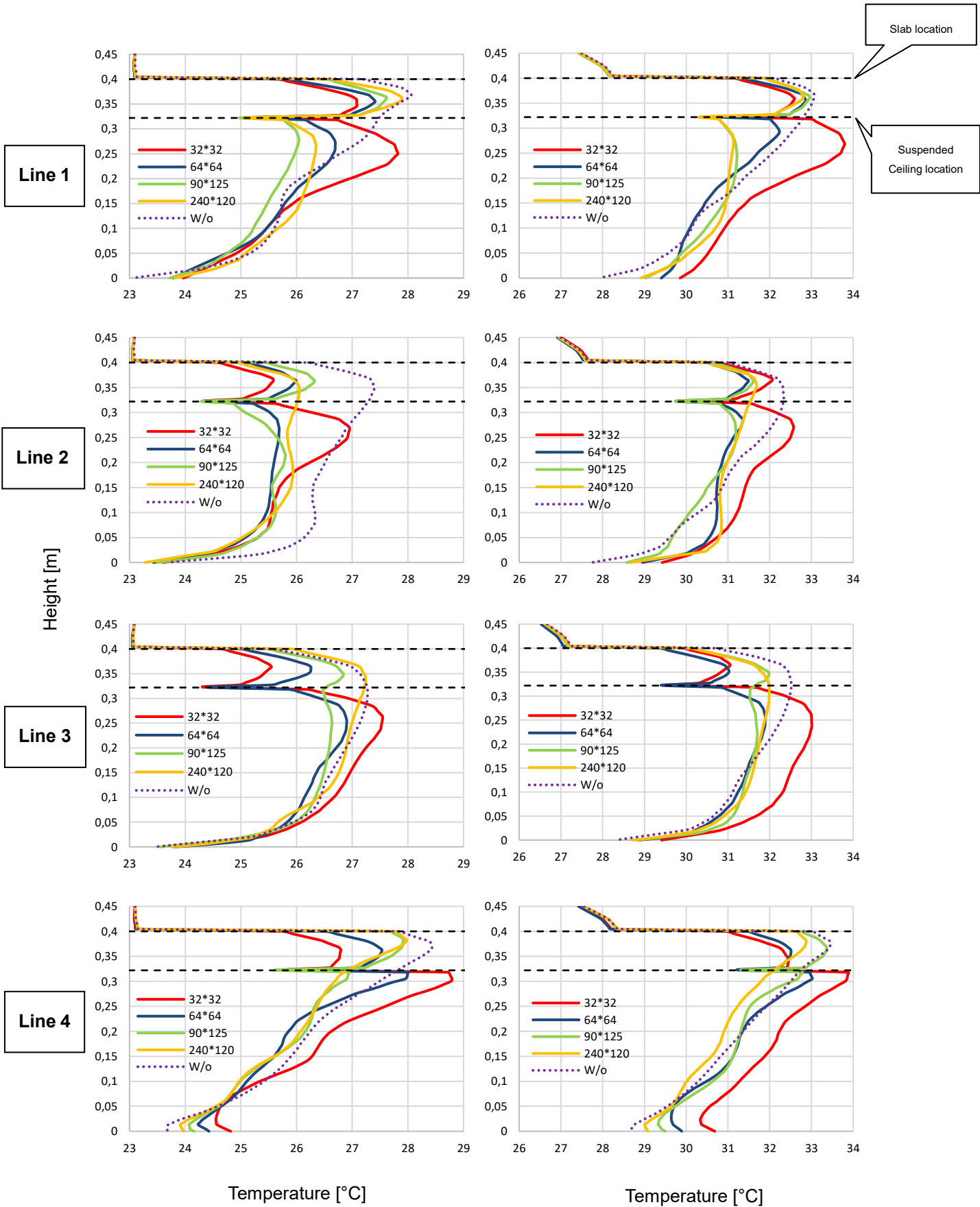
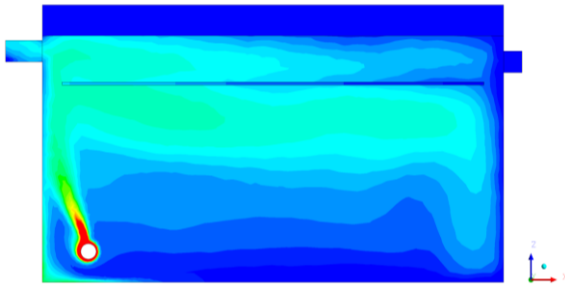


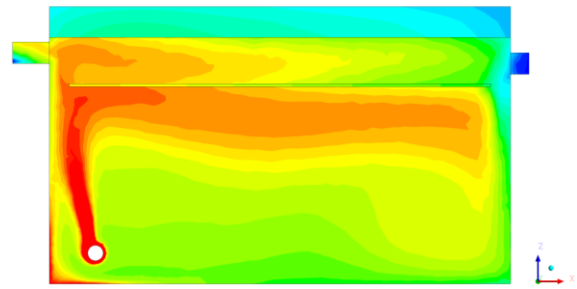
Figure 6.15 - Vertical temperature profiles along the four measurement lines for 5 minutes of operation time (HP), with the 5 different design scenarios.

Figure 6.16 - Vertical temperature profiles along the four measurement lines for 12 hours of operation time (HP), with the 5 different design scenarios.

Scenario 1 (32mm × 32mm)

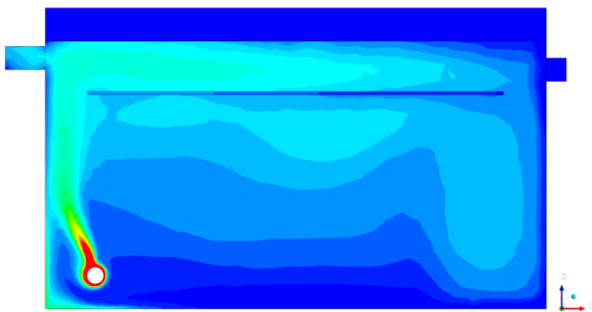


(a) t= 5m HP

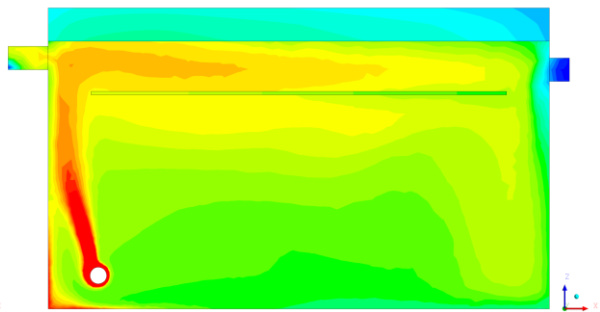


(b) t= 12h HP

Scenario 2 (64mm × 64mm)

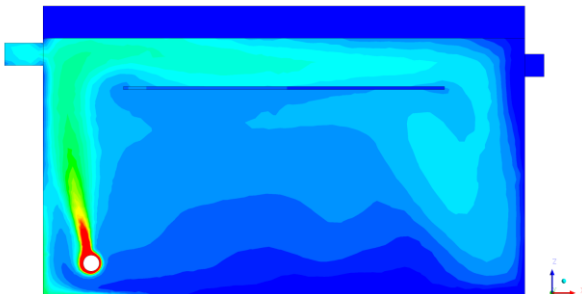


(c) t= 5m HP

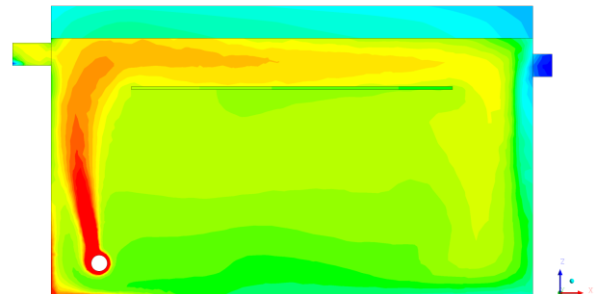


(d) t= 12h HP

Scenario 3 (90mm × 125mm)

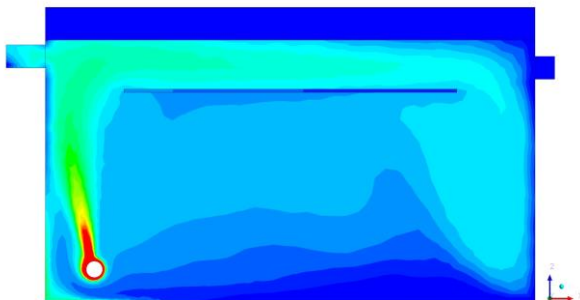


(e) t= 5m HP

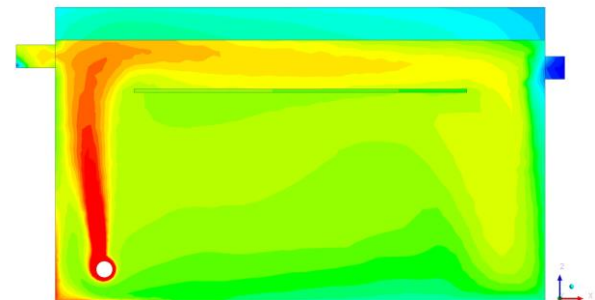


(f) t= 12h HP

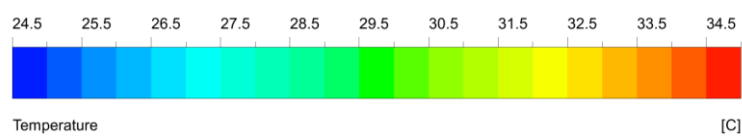
Scenario 4 (240mm × 120mm)



(g) t= 5m HP



(h) t= 12h HP



Scenario 6 (Without Suspended Ceiling)

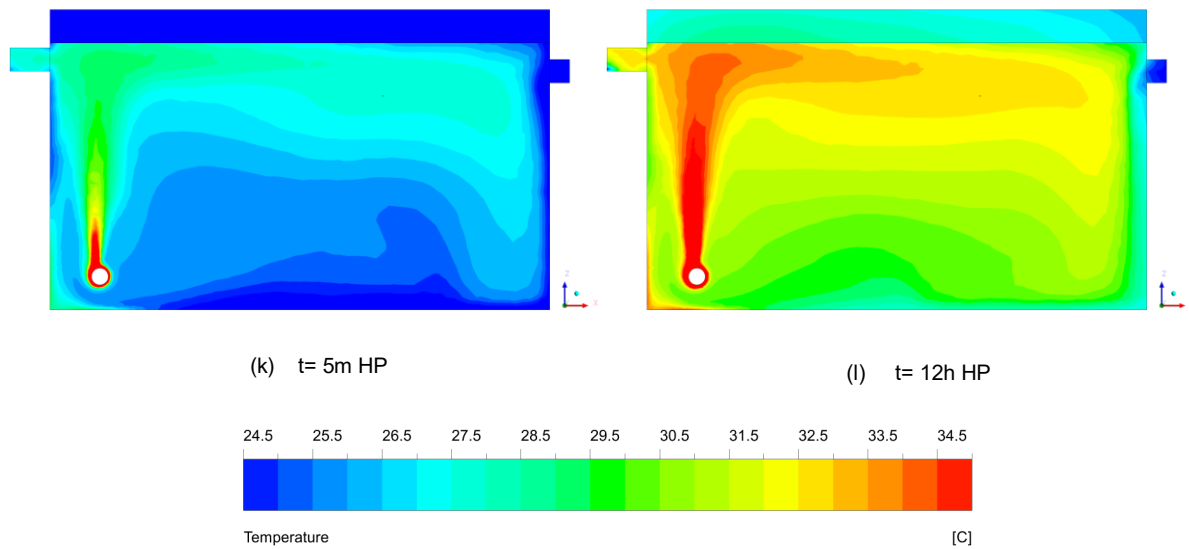


Figure 6.17 - Temperature contours for the different 5 scenarios

Table 6.1 - Results of the fluid mean temperature and the mass flow rate at the slots in two heating periods for the different scenarios.

	Sc1		Sc2		Sc3		Sc4		Sc6	
	32 × 32 (mm)		64 × 64 (mm)		90 × 125 (mm)		240 × 120 (mm)		W/o	
Time	5 m	12 h	5 m	12 h	5 m	12 h	5 m	12 h	5 m	12 h
\bar{T} [K]	28.15	33.838	27.937	33.235	28.028	33.219	28.203	33.188	28.369	33.211
\dot{m} [g/s]	0.2243	0.2221	0.2597	0.3295	0.319757	0.35607	0.285919	0.353442	0.3628	0.3451

We can conclude from the Figure 6.17, that the size of the suspended ceiling gaps controls the air flow pattern of the thermal plume. And by analysing all the previous results, the performance for the gap configuration of 90 × 125mm shows better agreement (lower values for the vertical lines as well for the average fluid temperature) in thermal comfort on occupation zone.

7 Conclusions and Future Work

7.1 Conclusions

The purpose of this study was to investigate the accuracy of CFD modelling of building ventilation flows driven by natural forces, and mechanical forces; and by evaluating the performance of multiple design scenarios for the suspended ceiling in a reduced scale model of an office with the aim of improving thermal comfort.

Comparisons were made between the theoretical CFD calculations (using RNG k-epsilon model) and the experimental measurements for a heating period of 12 hours. The temperature in the overall model for the CFD calculations were slightly higher ($\sim 2^{\circ}\text{C}$) and exhibited a different overall behaviour at the start of the heating period because we defined the external wall boundary condition as convection, and it seemed that the experimental data was losing the same amount of energy regardless of working conditions. For that reason, it is reasonable to assume a constant heat flux loss to simulate experimental data.

The influence of the ambient temperature on CFD calculations was studied with the aim of explain the temperature peak in the last 2 hours of the experimental data, and it was concluded that the data does not have any relation with laboratory temperature.

The efficiency of night cooling was tested, and depends directly on power of the heat source during the day period, the air flow rate during the night period, and the thermal capacity of the slab. It was found that the slab core temperature drops 4.5 degrees in only 6 hours night cooling operation exhibiting how this technique is effective.

The size of the suspended ceiling gaps controls the air flow pattern of the thermal plume and the mass flow rate in the inlet/outlet slots. Wider gaps between the suspended ceiling and the walls promote better heat exchange ratios and contribute to involve the slab in the passive technique of cooling. Also, it was concluded that this latter plays an important role in the attenuation of indoor peak temperatures.

The configuration with the best performance in thermal comfort is the scenario for the gap of $90 \times 125\text{mm}$.

Summing up, CFD offered good qualitative and quantitative results and to have buildings with better indoor environment and less energy consumption, good designs combined with high efficiently natural ventilation and mechanical ventilation are critical.

7.2 Future work

The results obtained with this thesis are just a base for future developments. Some topics that could give continuation to this work are:

- Only one localized point heat source exists in this thesis. In a real ventilated space of a building, there may have more heat sources and the sources may have different shapes with various areas. Therefore, more sophisticated benchmarks need to be defined in order to widen the use of CFD for natural ventilation modelling.
- The airflow in real naturally ventilated buildings is far more complex and is impractical to model using analytical techniques. Experiments on small scale structures are one method to understand the ventilation performance. However, this can be time consuming, and difficulty to modify. Therefore, it is often desirable to use CFD to model real buildings at the design stage to provide knowledge of building ventilation performance because it is relatively easy to investigate on variety of scenarios.
- Further work is needed to evaluate the accuracy of the boundary conditions.
- Combine the design scenario with different suspended ceiling properties.
- Study of night ventilation in the case of full coverage.

8 References

- [1] P. G. F. Branquinho, “Modelos de Previsão do Consumo Energético no Sector Residencial,” *PhD Thesis, IST Lisbon*, p. 93, 2014.
- [2] A. S. of H. R. and A. Engineers, “Thermal Environmental Conditions for Human Occupancy,” pp. 127–520, 2003.
- [3] A. Kayne, “Computational Fluid Dynamics (CFD) Modeling of Mixed Convection,” *PhD Thesis, Washingt. Univ.*, p. 70, 2012.
- [4] P. Höppe and I. Martinac, “Indoor climate and air quality,” *Int. J. Biometeorol.*, vol. 42, no. 1, pp. 1–7, 1998.
- [5] L. M. Tam, V. K. Sin, S. K. Lao, and . F. Choi, “CFD Analysis of Fire in a Forced Ventilated Enclosure,” vol. 2, Tsinghua, pp. 1–52, 2014.
- [6] C. E. Walker, “Methodology for the evaluation of natural ventilation in buildings using a reduced-scale air model,” *PhD Thesis, Massachusetts Inst. Technol.*, p. 211, 2006.
- [7] H. Mohd Yunus, H. Nasution, A. Abdul Aziz, Sumeru, and A. A. Dahlan, “The Effect of Ambient Temperature on the Performance of Automotive Air-Conditioning System,” *Appl. Mech. Mater.*, vol. 819, pp. 221–225, 2016.
- [8] V. Geros, M. Santamouris, S. Karatasou, A. Tsangrassoulis, and N. Papanikolaou, “On the cooling potential of night ventilation techniques in the urban environment,” *Energy Build.*, vol. 37, no. 3, pp. 243–257, 2005.
- [9] V. Dietz and N. Ward, *Oxford Textbook of Neurorehabilitation*. Press, Oxford University, 2015.
- [10] Y. C. Houghten FC, “Determination of the comfort zone, Thermal Booklet,” *ASHVE*, vol. 29, pp. 165–176, 1923.
- [11] G. Paliaga and P. F. Alspach, “Thermal Environmental Conditions for Human Occupancy,” vol. 1, ASHRAE., p. 54, 2013.
- [12] B. W. Olesen, M. Scholer, and P. O. Fanger, “Discomfort casued by vertical air temperature differences,” *Indoor Climate*. pp. 561–579, 1979.
- [13] M. J. Cook, “An Evaluation of Computational Fluid Dynamics for Modelling Buoyancy- Driven Displacement Ventilation,” *PhD Thesis, Univ. Leicester*, p. 264, 1998.
- [14] P. F. Linden, G. F. Lane-Serff, and D. A. Smeed, “Emptying filling boxes: the fluid mechanics of natural ventilation,” *J. Fluid Mech.*, vol. 212, no. 1, p. 309, 1990.
- [15] S. D. Fitzgerald and A. W. Woods, “On the transition from displacement to mixing ventilation with a localized heat source,” *Build. Environ.*, vol. 42, no. 6, pp. 2210–2217, 2007.

- [16] C. Zhang, M. H. Kristensen, J. S. Jensen, P. K. Heiselberg, R. L. Jensen, and M. Pomianowski, "Parametrical analysis on the diffuse ceiling ventilation by experimental and numerical studies," *Energy Build.*, vol. 111, pp. 87–97, 2016.
- [17] Y. Ji, M. J. Cook, and V. Hanby, "CFD modelling of natural displacement ventilation in an enclosure connected to an atrium," *Build. Environ.*, vol. 42, no. 3, pp. 1158–1172, 2007.
- [18] F. Durrani, M. J. Cook, J. J. Mcguirk, N. B. Kaye, and B. Engineering, "CFD Modelling of plume interaction in natural ventilation," *12th Conf. Int. Build. Perform. Simul. Assoc. Sydney*, pp. 14–16, 2011.
- [19] Q. Chen, "Comparison of different $k-\epsilon$ models for indoor air flow computations," *Numer. Heat Transf. Part B Fundam.*, vol. 28, no. 3, pp. 353–369, 1995.
- [20] M. J. Cook, Y. Ji, and G. R. Hunt, "CFD modelling of natural ventilation: combined wind and buoyancy forces," *Int. J. Vent.*, vol. 1, no. 3, pp. 169–179, 2003.
- [21] J. Fan, C. A. Hviid, and H. Yang, "Performance analysis of a new design of office diffuse ceiling ventilation system," *Energy Build.*, vol. 59, pp. 73–81, 2013.
- [22] A. Sreshtaputra, J. Haberl, and M. J. Andrews, "Improving building design and operation of a Thai Buddhist temple," *Energy Build.*, vol. 36, no. 6, pp. 481–494, 2004.
- [23] M. Kolokotroni, B. C. Webb, and S. D. Hayes, "Summer cooling with night ventilation for office buildings in moderate climates," *Energy Build.*, vol. 27, no. 3, pp. 231–237, 1998.
- [24] V. Geros, M. Santamouris, A. Tsangrasoulis, and G. Guarracino, "Experimental evaluation of night ventilation phenomena," *Energy Build.*, vol. 29, no. 2, pp. 141–154, 1999.
- [25] N. Artmann, H. Manz, and P. Heiselberg, "Parameter study on performance of building cooling by night-time ventilation," *Renew. Energy*, vol. 33, no. 12, pp. 2589–2598, 2008.
- [26] C. A. Balaras, "The role of thermal mass on the cooling load of buildings. An overview of computational methods," *Energy Build.*, vol. 24, no. 1, pp. 1–10, 1996.
- [27] M. Kolokotroni and A. Aronis, "Cooling-energy reduction in air-conditioned offices by using night ventilation," *Appl. Energy*, vol. 63, no. 4, pp. 241–253, 1999.
- [28] R. Høseggen, H. M. Mathisen, and S. O. Hanssen, "The effect of suspended ceilings on energy performance and thermal comfort," *Energy Build.*, vol. 41, no. 2, pp. 234–245, 2009.
- [29] Weitzmann P, "The cooling capacity of the Thermo Active Building System combined with acoustic ceiling," *8th Symp. Build. Phys. Nord. Countries. Copenhagen, Denmark.*, 2008.
- [30] "Dry Air Properties." [Online]. Available: http://www.engineeringtoolbox.com/dry-air-properties-d_973.html. [Accessed: 16-Sep-2017].
- [31] "Air Properties." [Online]. Available: <http://www.engineeringtoolbox.com/air-properties->

- d_156.html. [Accessed: 16-Sep-2017].
- [32] F. P. Incropera and D. P. Dewitt, *Fundamentals of Heat and Mass Transfer*. John Wiley & Sons, 2010.
- [33] FLUENT, *ANSYS FLUENT User's Guide*, vol. 10, no. 1. FLUENT Inc., 2013.
- [34] M. Lança, P. J. Coelho, and J. G. Viegas, "Enhancement of heat transfer in commercial buildings during night cooling - Reduced scale experimentation.," *9th World Conf. Exp. Heat Transf. Fluid Mech. Thermodyn. Brazil*, p. 3, 2017.
- [35] M. Lança, P. J. Coelho, and J. G. Viegas, "Enhancement of heat transfer in commercial buildings during night cooling - CFD study and reduced scale experimentation," *Congr. M. Numéricos en Ing. España*, p. 15, 2017.
- [36] M. Keating, "Accelerating CFD Solutions," *ANSYS Advant.*, pp. 47–49, 2011.
- [37] "Concrete Properties." [Online]. Available: https://www.engineeringtoolbox.com/concrete-properties-d_1223.html. [Accessed: 16-Sep-2017].
- [38] Isolparma, "EXPS Extruded Polystyrene Foam Boards." [Online]. Available: <http://www.isolparma.it/ted/pdf/XPS.pdf>. [Accessed: 16-Sep-2017].
- [39] F. Pracht, *Materials and the Environment*, vol. 19, no. 3. B&H, 2011.

9 Appendix

Appendix 1

Interpreted function of the Ambient Air for *FLUENT*:

```
DEFINE_PROFILE(unsteady_temperature, thread, position)
{
    face_t f;

    real t=CURRENT_TIME;

    begin_f_loop(f, thread)
    {
        F_PROFILE(f, thread, position) = 273.15+(24-1.2*sin(0.0000727221*t+2.8));
    }
    end_f_loop(f, thread)
}
```

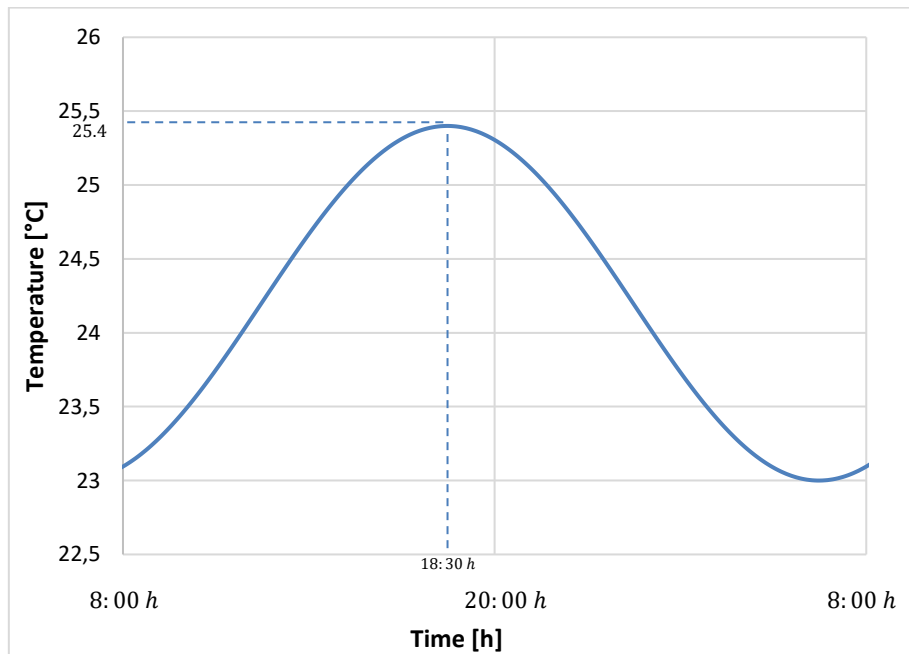


Figure 9.1 – UDF function, ambient temperature vs hour of the day

Appendix 2

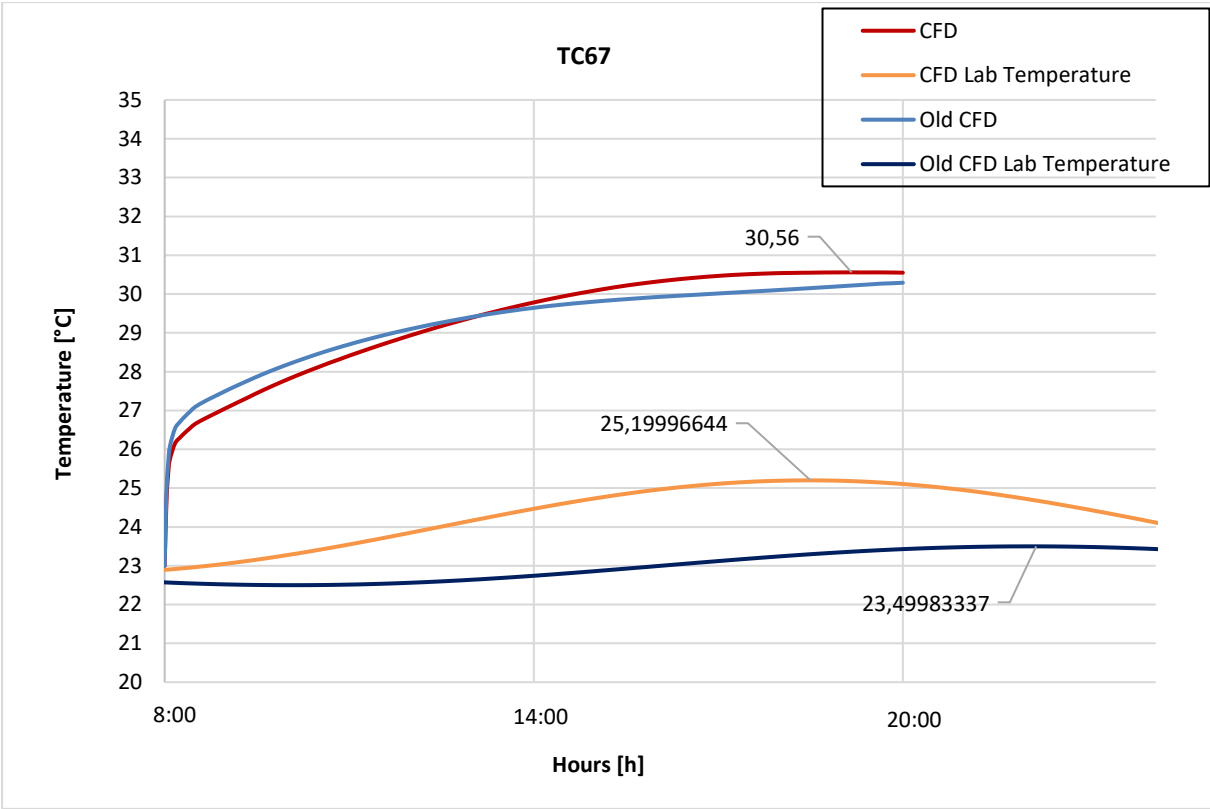


Figure 9.2 – Difference in the CFD temperature at Thermocouple 67 according to different ambient temperatures

In a first stage of this thesis, the simulations were performed according to a different ambient temperature (*Old CFD Lab Temperature*) resulting in the simulation of the blue line. The heat flux loss (side walls and floor) is, obviously, different from our case study (red line) and has a value of -6.2 W/m^2 . We can see that the temperature of this latter simulation keeps rising due to the increase of the ambient temperature.

For our case study, the time delay between the maximum CFD temperature (Red) and the maximum Lab temperature (Yellow) is about **36 minutes**.